POLITECNICO
MILANO 1863

SCUOLA DI INGEGNERIA INDUSTRIALE
E DELL'INFORMAZIONE

Study on Segmentation Techniques for Geometric Measurements in Industrial Computed Tomography

TESI DI LAUREA MAGISTRALE IN
AUTOMATION AND CONTROL ENGINEERING - INGEGNERIA DELL'AUTOMAZIONE

Author: **Federico Pirillo**

Student ID: 970896
Advisor: Prof. Giovanni Moroni
Co-advisor: Prof. Stefano Petrò, Dr. Huan Shao
Academic Year: 2022-2023

Abstract

X-ray computed tomography (XCT) is a non-destructive technique that has gained significant importance, particularly in the context of additive manufacturing. With the ability to capture detailed information about complex-shaped parts, XCT offers valuable insights that conventional measuring systems often struggle to provide. However, the XCT process involves multiple steps, each contributing to uncertainties. One crucial aspect are the segmentation techniques, which focuses on distinguishing different materials or regions of interest within the scanned object. Despite the availability of numerous segmentation algorithms in the literature, there is a lack of standardization and guidelines for selecting the most appropriate method for specific scenarios.
This thesis aims to bridge this gap by conducting a comprehensive review of existing research on segmentation in industrial XCT. By examining the state of the art we sought to gain a deeper understanding of the current landscape, including the methods employed and the research groups involved. Subsequently, we identified a set of commonly used segmentation methods in XCT and performed a comparative analysis among them. To facilitate this analysis, an aluminum stepped cylinder was utilized as a test object, and evaluations were conducted based on three distinct features: diameter, cylindricity, and height. Furthermore, we propose a subvoxeling technique that leverages Taylor Expansion series up to the third order to refine the measurement accuracy of the segmentation methods at a subvoxel level.
The results of the comparisons demonstrated varying behaviors among the applied methods depending on the specific feature of interest and the chosen scan conditions and parameters. Notably, the subvoxeling technique exhibited remarkable efficacy, particularly in the case of cylindricity, surpassing both other methods and those that inherently incorporate subvoxeling. Overall, this thesis contributes to the understanding of segmentation in industrial XCT by comprehensively surveying the existing literature, identifying commonly employed methods, and conducting comparative evaluations.

Keywords: Industrial Computed Tomography, Geometric Measurement, Segmentation Technique, Subvoxeling Technique

Abstract in lingua italiana

La tomografia computerizzata a raggi X (XCT) è una tecnica non distruttiva che ha acquisito un'importanza significativa, in particolare nella produzione additiva. Con la capacità di catturare informazioni dettagliate su parti di forma complessa, la XCT offre una visione che i sistemi di misurazione convenzionali spesso faticano a fornire. Tuttavia, il processo di XCT coinvolge molteplici fasi, ciascuna delle quali contribuisce a incertezze. Un aspetto cruciale sono le tecniche di segmentazione, che si concentrano sulla distinzione di materiali diversi o regioni di interesse all'interno dell'oggetto scansionato. Nonostante l'esistenza di numerosi algoritmi di segmentazione nella letteratura, manca una standardizzazione e linee guida per selezionare il metodo più adatto per scenari specifici. La tesi si propone di colmare questa lacuna mediante una revisione delle ricerche esistenti sulla segmentazione nella XCT industriale. Esaminando lo stato dell'arte, compresi i metodi impiegati e i gruppi di ricerca coinvolti, abbiamo cercato di ottenere una comprensione più approfondita del panorama attuale. Successivamente, abbiamo identificato un insieme di metodi di segmentazione comunemente usati nella XCT e abbiamo effettuato un'analisi comparativa tra di essi. Per agevolare questa analisi, è stato utilizzato un cilindro gradinato in alluminio come oggetto di prova, e sono state condotte valutazioni basate su tre distinte caratteristiche: diametro, cilindricità e altezza. Inoltre, proponiamo una tecnica di "subvoxeling" che sfrutta la serie di espansione di Taylor fino al terzo ordine per affinare l'accuratezza di misurazione dei metodi di segmentazione a livello di "subvoxel". I risultati delle comparazioni mostrano comportamenti variabili tra i metodi applicati a seconda della caratteristica considerata e delle condizioni e parametri di scansione scelti. In particolare, la tecnica di "subvoxeling" ha dimostrato un'efficacia notevole, soprattutto nel caso della cilindricità, superando sia gli altri metodi sia quelli che incorporano intrinsecamente il "subvoxeling". In generale, questa tesi contribuisce alla comprensione della segmentazione nella XCT industriale mediante una revisione completa della letteratura esistente, l'individuazione dei metodi comunemente impiegati e la conduzione di valutazioni comparative.

Parole chiave: Tomografia Computerizzata Industriale, Misurazione Geometrica, Tecnica di Segmentazione, Tecnica di Subvoxeling

Contents

1 | Introduction

The first appearance of the X-Ray Computed Tomography (XCT) machines dates back to 1971 in a medical application with the first patient brain scan performed in Wimbledon, UK [1, 2]. Then, since 1980, it became popular for material analysis and first non-destructive tests (NDT), allowing to observe the inner structure of materials and detecting defects [3]. As far as dimensional metrology is concerned, the first attempt dates back to 1991 (with low accuracy, no better than 0.1mm) [4]. The breakthrough came in 2005 with the dedicated dimensional XCT machine exhibited at the Control Fair in Germany.
The advantage of this technology is to be able to visualize and measure both the inner and outer features of an object without having to cut it through and destroy it, also allowing the performing of dimensional quality control and material quality control simultaneously.
For these reasons, it is very important for the industrial quality control of workpieces having non-accessible internal features (e.g. additive manufactured components) or multi-material components.

Even if the dimensional metrology field shares the same physical and mathematical principles, the procedures are quite different with respect to the other fields of application. In the medical application, in fact, the doses of the radiation (power) have to be limited to protect the patient, just as it cannot be rotated the same way as mechanical workpieces. In addition, the requirement on accuracy and spatial resolution are relatively low [5]. As we said, XCT is a relatively new technique for industrial dimensional metrology. Combined with the fact that to model the attenuation of X-rays through a material is a complex problem, as a result there are no currently international standards to guide uncertainty estimation. Current initiatives for uncertainty estimation are typically based on comparison with calibrated objects and other approaches like simulation and statistical methods.

1.1. Basic Principles

A source emits X-rays which then pass through the material of the workpiece. During this process, the X-rays are attenuated due to either absorption or scattering. The extent of attenuation depends on factors such as the distance traveled through the absorbing material, the composition and density of the material, and the energy of the X-rays. To quantify this attenuation, the remaining X-rays that pass through the workpiece are captured using an X-ray detector. This yields a 2D gray-scale image, particularly when using a flat panel detector. Multiple images are taken from different angles around the workpiece. By mathematically reconstructing these projected images, a 3D voxel model is created. In this model, the gray value of each voxel represents the material's level of attenuation
Subsequent steps involve identifying the workpiece's cloud of points through segmentation, followed by dimensional measurement and quality control[5].

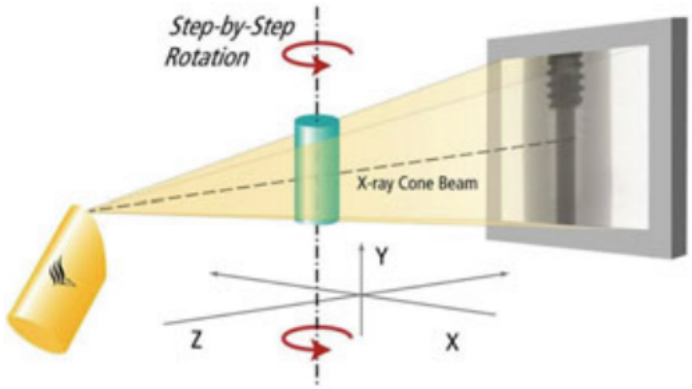

Figure 1.1: Cone-beam with 2D flat panel detector [6]

1.2. X-rays

X-rays are produced by accelerating electrons through a high voltage and allowing them to collide with a metal target. X-rays are produced through two distinct processes: bremsstrahlung and characteristic radiation. Bremsstrahlung is caused when an electron approaches very close to the nucleus of an atom but does not actually collide with any part of it. In fact, when high-energy electrons pass through a material, such as a metal target, they experience the electromagnetic force from the positively charged atomic nuclei. This interaction causes the electrons to change direction and lose energy. As a result of this sudden deceleration, the electrons emit a radiation, known as bremsstrahlung

radiation, which is characterized by a continuous spectrum and and constitutes the dominant production of X-rays in the process. Characteristic radiation is caused when the high-energy electrons collide directly with one of the shell electrons, creating an electron vacancy. When this vacancy is filled with an electron from an outer shell, a discrete spectrum of X-rays is emitted. This type of radiation takes the name from the fact that it is a property of the target material, depending on the atomic number of the target. It produces energy spikes that are superimposed onto the continuous radiation.

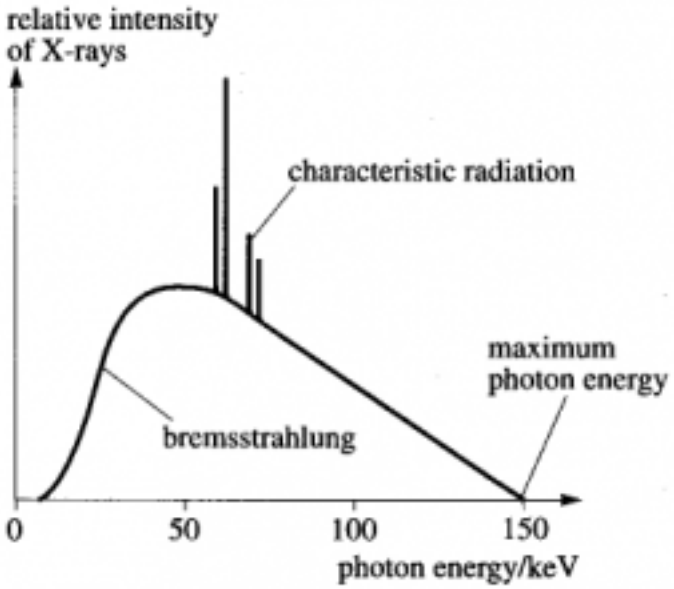

Figure 1.2: X-ray radiation spectrum [7]

The generated X-ray radiation is characterized by its energy distribution (also called quality) and its intensity (flux). The highest-energy present in the X-ray spectrum determines the penetrating power of the X-ray beam into matter. The intensity of an X-ray beam is a measure of the amount of radiation energy flowing per unit of time. [8].

1.3. System and components

The objective of this section is to present a comprehensive overview of the primary elements comprising an XCT machine. Specifically, our focus will be on:

- Source
- Detectors
- Kinematic System

- Software

1.3.1. X-ray sources

The X-ray source consists of the following elements:

- *Thin Filament (Cathode)*: Typically composed of tungsten, the thin filament produces electrons through thermionic emission, which occurs when the filament is electrically heated.
- *Target (Anode)*: The target is made of tungsten and copper, known for its high melting point.
- *Vacuum Environment*: The X-ray source is maintained in a vacuum environment to prevent interactions with gas molecules.
- *Window*: Located at the exit of the X-ray tube, the window consists of either a circular aperture (for cone beam) or collimating plates (for fan beam). Its purpose is to shape the X-ray beam that will interact with the workpiece [7].

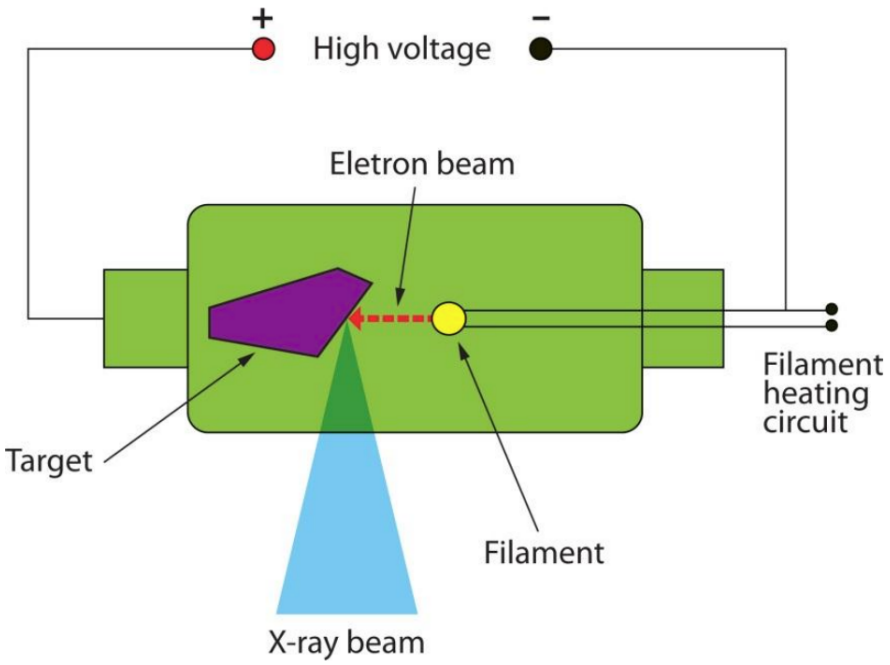

Figure 1.3: Structure of a typical X-ray source [7]

The electrons emitted by the cathode are accelerated towards the anode through an electric potential. Upon reaching the anode, they collide with the atoms in the target, causing a sudden deceleration. This collision results in the conversion of energy into heat and X-rays.

1.3.2. X-ray detectors

The most commonly used detectors nowadays are indirect flat panel detectors (FPD). These detectors are equipped with a scintillator coating that facilitates the conversion of high-energy X-ray photons into lower energy photons within the visible wavelength range. Subsequently, a photodiode is employed to detect the visible light and convert it into a digital output.

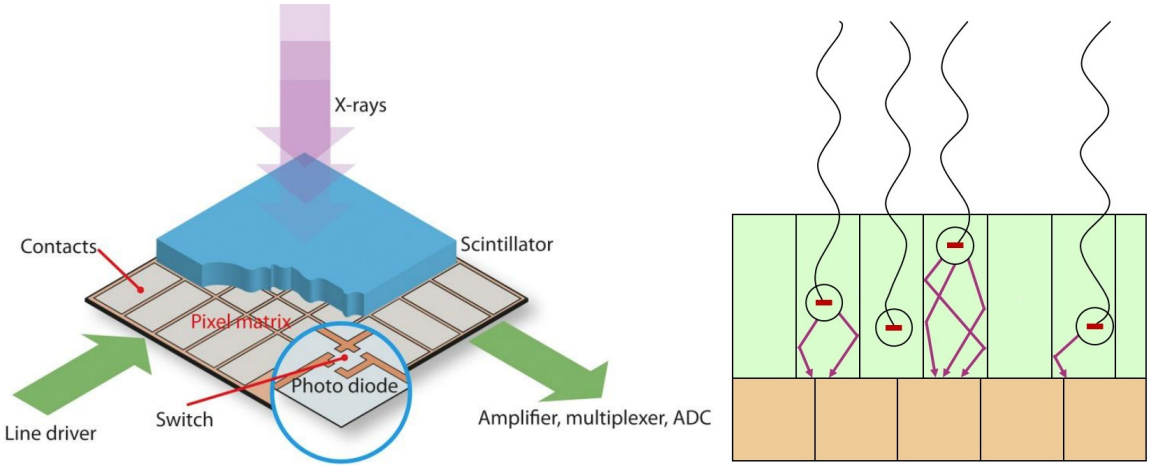

Figure 1.4: Structure of a scintillation detector [9]

1.3.3. Kinematic systems

In an industrial XCT machine, the object of interest is positioned between the X-ray source and the detector. To capture images from various perspectives, the object undergoes rotation. The kinematic system commonly employed for this purpose typically consists of the following components:

- *Turntable*: This component enables the rotation of the workpiece, allowing for the acquisition of images from different angles.
- *Horizontal Translation Axis*: The horizontal translation axis is responsible for positioning the turntable. Additionally, it can be utilized for geometrical magnification, where adjusting the distance between the object and the source results in higher resolution.
- *Vertical Translation Axis*: The vertical translation axis is used for positioning the workpiece. In the case of 1D detectors, this axis also facilitates the scanning of different slices.

1.3.4. Software

Once the images have been captured by the detector for each rotational position, they undergo a series of computations that convert the collected information into voxel data. In this process, the software used plays a crucial role, particularly in the reconstruction of a volumetric model from the acquired 2D projection images. The software employs algorithms and techniques to reconstruct a three-dimensional representation of the object under examination. This step is vital in transforming the acquired image data into a comprehensive volume model that can be further analyzed and visualized for various applications.

1.4. Workflow for dimensional metrology

The dimensional metrology process in XCT imaging involves two types of steps: physical measurement and subsequent data processing.

Physical measurement involves the use of a XCT machine to conduct a series of x-ray scans on the object of interest. These scans generate grayscale images that are captured by the detector. The process results in an ordered collection of images, that can be utilized for subsequent measurements of the object's characteristics and features. This collection of images serves as the basis for further analysis and measurements. During this step, various parameters must be carefully considered due to their influence on the X-ray imaging process. These parameters include the source current, source voltage, number of projection images per pose, and the type of target used, among others. Additionally, scale identification is performed as a calibration step to establish a global scale factor that links the voxel size to the unit of length. This step is important for determining the position of the magnification axis and is typically achieved by measuring a simple calibrated reference object.

On the other hand, the aim of the processing steps is to extract the required point cloud information starting from the acquired gray images. These processing steps are crucial for transforming the raw image data into a usable form, enabling the further analysis of dimensional measurands. The main steps involved in this process are reconstruction, segmentation, and feature extraction from the point cloud. The first major step is reconstruction. This involves utilizing the back-projection algorithm to generate a voxel-based representation of the part based on the XCT projection images. After the reconstruction, the next step in the process is the application of segmentation techniques. Segmentation techniques typically involve three key steps: noise reduction, segmenta-

tion, and subvoxeling. Noise reduction is an optional step that aims to filter out any noise present in the original data, enhancing the quality of the subsequent segmentation. Segmentation is then performed to identify and separate the object of interest from the surrounding background or other structures within the XCT volume. This step enables the isolation of the specific region or object for further analysis or measurement. Finally, the subvoxeling technique is introduced to refine the segmentation results by adjusting the identified points to be closer to the actual surface of the object. This refinement helps improve the accuracy and precision of the dimensional measurements obtained from the XCT data. These methods often originate from image processing and sub-pixeling techniques. A review of the current state of these methods in image processing can be found in the work by Jing, Junfeng, et al. (2022) [10]

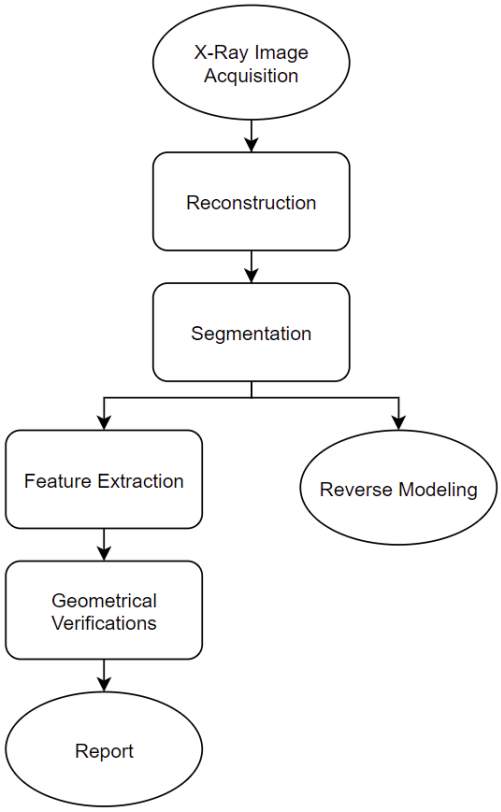

Figure 1.5: Steps in X-ray Computed Tomography for metrology

After the segmentation process, industrial XCT analysis typically branches into two paths: geometrical verifications and reverse modeling. This thesis will focus on the geometrical verifications path.

After obtaining the points of the surface, precise identification of the measuring points and their corresponding coordinates is necessary. These points represent the measurand, such as the dimensions to be measured or the features of interest. Once the measurand

is identified, it can be measured, and the analysis and comparisons are performed to assess the results.

1.5. Objective of the thesis

Despite the significant progress made in the field, there are still several challenges that need to be overcome. One of the major limitations is the absence of a standardized procedure on how to proceed with segmentation and determine the most suitable method for a given application. Researchers often face the problem of choosing from a wide range of segmentation algorithms without clear guidelines or benchmarks to guide their decision-making process. This lack of standardization makes it difficult to compare and evaluate different methods objectively.

Another limitation in the current literature is the insufficient depth of comparative studies among segmentation methods. While individual research papers often demonstrate the effectiveness of a specific algorithm or propose novel techniques, there is a lack of comprehensive comparisons that assess the performance of various segmentation methods. This gap prevents researchers and potential industrial users from gaining a comprehensive understanding of the strengths and weaknesses of different segmentation approaches and limits their ability to make informed choices.

Given these limitations, the objectives of this thesis can be summarized as follows:

- Conduct a thorough literature review that classifies the methods employed in segmentation analysis.
- Perform a comprehensive comparison of the identified common methods found in the literature.
- Propose a subvoxeling technique to improve the overall accuracy of the segmentation results.

By accomplishing these objectives, this research aims to contribute to the advancement of segmentation analysis in X-ray Computed Tomography. The findings of this thesis will provide valuable insights into the strengths and weaknesses of different segmentation methodologies across different features.

1.6. Organization of the thesis

This thesis work focuses on investigating the impact of the segmentation step in X-ray Computed Tomography. It is structured into six chapters.

Chapter 2 presents a comprehensive review of the current state of the art in segmentation techniques and discusses the main challenges associated with the topic. It includes the literature research conducted to identify typical methods used in metrology and their classification, active research groups in the field, and the evaluation methods commonly employed.

Chapter 3 describes the experimental setup in detail. This includes the XCT machine used, the specimen under investigation, the evaluated features, the software processing steps for data preparation, the chosen segmentation methods, their implementation using MATLAB software, and the extraction and measurement of features.

Chapter 4 presents the results obtained from the segmentation process and provides relevant observations and analysis.

Finally, Chapter 5 summarizes and discusses the overall findings and achievements of the research. It also includes a discussion on future work and potential improvements in the field.

2 | State of the art

The objective of this thesis chapter is to provide a comprehensive overview of works related to segmentation. The chapter aims to cover various aspects, starting from the definition of segmentation and progressing to a brief classification of segmentation methods. Additionally, the chapter presents a summary of contributions made in the field of segmentation, highlighting the most commonly applied methods and their distribution among a set of reviewed papers.

The chapter is structured as follows:

- In Section 2.1, an introduction to the topic of segmentation is provided, along with its definition.
- Section 2.2 outlines the research methodology employed to conduct a comprehensive review of the current state of the art in the segmentation for Industrial Computed Tomography. It discusses the process of searching and identifying relevant research papers, as well as the creation of a classification map based on the identified methods.
- Section 2.3 focuses on the conclusions of the literature review conducted, analyzing the most frequently used methods, active research groups, and their workflow in the field of segmentation.

By following this chapter structure, readers will gain a comprehensive understanding of segmentation, its classification, and the state of the art in this field.

2.1. Segmentation

Segmentation plays a critical role in processing XCT images by dividing an image or volume into multiple regions. This process is essential for identifying and isolating interior or exterior regions of interest within a scanned specimen.
In metrology applications, once the 3D model has been reconstructed, it becomes necessary to separate the object from the surrounding background or, in the case of multiple

materials, to distinguish between different materials. The resulting segmentation serves as a foundation for various calculations, including the determination of lengths, diameters, and shape factors of the targeted features. It also provides an initial estimation of component regions and their boundaries, which can be further refined in subsequent steps such as surface determination. This preliminary segmentation step is crucial in enabling accurate analysis and measurement of the scanned specimen [11].
The impact of segmentation on the accuracy of dimensional measurements in surface determination is an actively researched topic [12–15]. In current X-ray XCT metrology applications, the most commonly used methods are Otsu-based thresholding [16] and local adaptive thresholding techniques. However, alternative approaches such as Canny-based algorithms [17, 18] can also be found for surface determination [19].

The limitations in image quality and the occurrence of local boundary errors in segmentation algorithms can be attributed to several main factors. These include image artifacts such as beam hardening, scattering, and cone-beam effects, as well as errors arising from image scaling, finite voxel discretization, and noise [20].

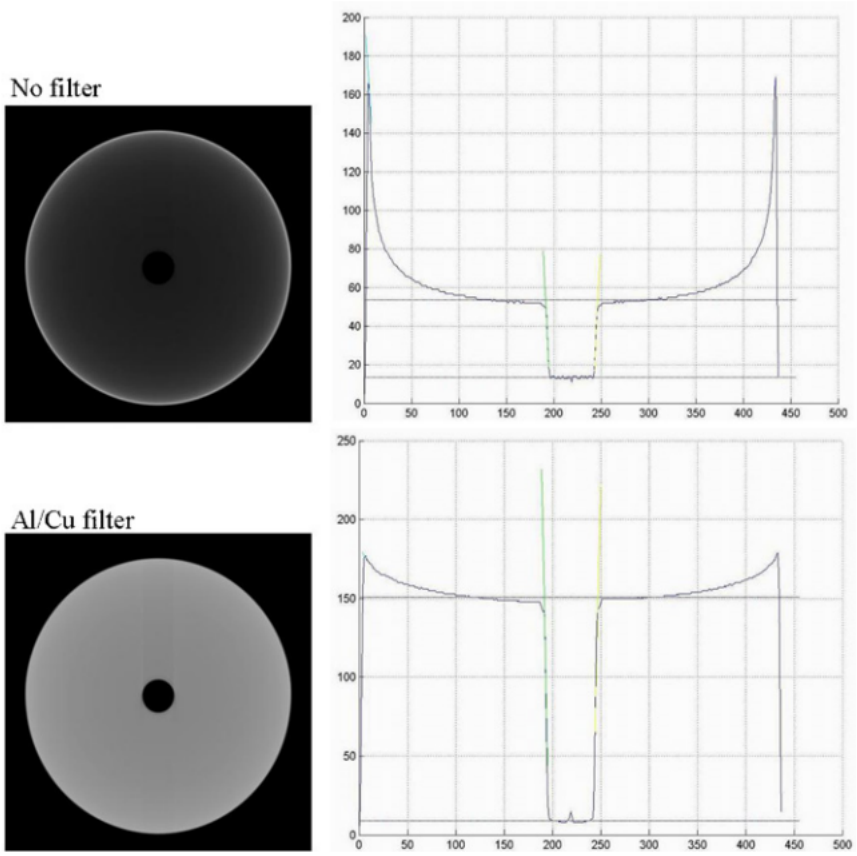

Figure 2.1: Example of beam hardening artifact on the X-ray image of a hollow cylinder [5]

These effects can introduce distortions and inaccuracies in the segmentation process, impacting the overall quality of the resulting image and potentially affecting the accuracy of subsequent measurements and analyses.

The fundamental issue is that the presence of artifacts in the XCT data modify the spatial grey values of the reconstructed images and as a result, degrades their quality and affects the accuracy of dimensional measurements based on such data. The definition of the term 'artifact' is given in ISO 15708-1 [21] as: the discrepancy between the actual value of some physical property of an object and the map of that property generated by a XCT imaging process.

A summary of XCT artifacts commonly encountered in metrology applications is presented in Table 2.1.

Artifacts in XCT	
Name	Cause
Beam Hardening	Low energy radiation part of the X-ray spectrum attenuates at a faster rate than the high energy portion. However, most of the current reconstruction algorithms assume beam monochromaticity, which leads to errors in the XCT data.
Scatter radiation	X-ray photons that deviate from the line connecting source-to-detector may hit the detector in unexpected cell locations, increasing photon count at these detector cells.
Partial volume	Caused by limited field of view of the XCT system. The attenuation coefficients in the volume cannot be calculated properly due to missing information.
Ring artifact	Defective or uncalibrated detector elements that generates 'noise-like' rings centered at the XCT rotation axis.

Table 2.1: Description of XCT artifacts [22]

2.2. Literature review

To make this literature review, a comprehensive selection process was employed. The initial step involved gathering a large number of papers through a systematic search on the Scopus database. The search was performed using specific keywords related to segmentation in industrial computed tomography. The keywords used included "segmentation," "surface determination," "surface extraction," "edge detection," and "threshold." The search was limited to English language papers and excluded studies related to diseases and clinical applications.

From the initial set of papers obtained, a rigorous screening process was done to select the most relevant ones for further analysis. The selection criteria primarily focused on papers related to segmentation in industrial computed tomography, particularly those involving monomaterial metallic parts. Additionally, the papers were assessed based on their emphasis on metrology rather than defect analysis.

After this screening process, approximately 60 papers were identified as highly relevant and chosen for detailed examination. These papers formed the basis for extracting a satisfactory collection of segmentation methods currently applied in the state of the art. Tables 2.2-2.4 presents the collection of papers found in the literature.

The selected papers were thoroughly analyzed to identify the segmentation methods employed and to determine the main research groups working in this area. To categorize and visualize the distribution of these methods, a classification map was created (Figure 2.2). This map divided the methods into macro classes, highlighting the most prominent ones.

A comprehensive description of each method within these macro classes is provided below:

- **Threshold-based** methods involve selecting a threshold value to separate objects or regions of interest based on intensity values. Global thresholding applies a single threshold value to the entire image or volume, assuming that the intensity values of objects and background can be separated by a single threshold. In contrast, local thresholding adjusts the threshold value for each voxel based on its local neighborhood, taking into account spatial information and intensity variations within smaller regions.By adapting the threshold locally, this technique can handle images with varying illumination or intensity gradients more effectively. Both global and local thresholding techniques have their advantages and limitations, and the choice of method depends on the specific characteristics of

Threshold-based			
Title	**Year**	**Country**	**Method**
Sub-pixel high precision dimensional measurement method for aero-engine hollow turbine blade based on industrial computed tomography image [23]	2022	China	Otsu
Adaptive surface geometry determination in multi-material x-ray computed tomography using fringe projection [24]	2022	Germany	Local Adaptive
Analysis and experiment of effective factors in industrial CT dimensional measurement [25]	2021	China	Otsu, Phansalkar, FCM, MMPSO, NN
Surface extraction from micro-computed tomography data for additive manufacturing [26]	2021	USA	CL-Ridler+Local Adaptive
Qualification of CT data for areal surface texture analysis [27]	2019	France	Global thresholding
An interlaboratory comparison of X-ray computed tomography measurement for texture and dimensional characterisation of additively manufactured parts [28]	2018	UK	VGStudio
Comparison of surface extraction techniques performance in computed tomography for 3D complex micro-geometry dimensional measurements [29]	2018	Spain	Canny, Local Adaptive
A CBCT series slice image segmentation method [30]	2018	China	Phansalkar
A new threshold selection method for X-ray computed tomography for dimensional metrology [31]	2017	Poland	Threshold-based
Areal surface texture data extraction from X-ray computed tomography reconstructions of metal additively manufactured parts [32]	2017	UK	VGStudio
Precision Evaluation of the Reconstruction Model Based on Unigraphics [33]	2017	China	Otsu
Assessment of the Measurement Procedure for Dimensional Metrology with X-ray Computed Tomography [34]	2016	UK	VGStudio
Quantifying the Contribution of Post-Processing in Computed Tomography Measurement Uncertainty [35]	2016	Denmark	Local Adaptive
An Optimized Segmentation Algorithm for the Surface Extraction in Computed Tomography for Metrology Applications [36]	2015	Spain	Canny, Deriche, Local Adaptive
Accuracy study of a 450 KV CT system with a calibrated test object [37]	2013	Belgium	VGTudio
An image segmentation algorithm based on kernel estimation and moment-preserving [38]	2010	China	Threshold-based
Classification for volume rendering of industrial CT based on minimum cross entropy [39]	2007	China	Threshold-based
Classification for volume rendering of industrial CT based on moment of histogram [40]	2007	China	Threshold-based
Surface extraction from multi-material components for metrology using dual energy CT [41]	2007	Austria	Local Adaptive
Point cloud reconstruction with sub-pixel accuracy by slice-adaptive thresholding of X-ray computed tomography images [42]	2004	Switzeland	Adaptive-thresholding

Boundary-based			
Title	**Year**	**Country**	**Method**
High precision post-processing framework for industrial computed tomography detection [43]	2022	China	Multi-method combination (contour extraction)
Application of an edge detection algorithm for surface determination in industrial X-ray computed tomography [44]	2022	Germany	3D Prewitt+Median filter
Assessment of gradient-based algorithm for surface determination in multi-material gap measurements by x ray computed tomography [45]	2020	Spain	Canny, Deriche
Three-Dimensional Reconstruction of Continuous Tomographic ICT Images of Defective SRM [46]	2020	China	Edge-based methods
Comparison of surface extraction techniques performance in computed tomography for 3D complex micro-geometry dimensional measurements [29]	2018	Spain	Canny, Local Adaptive
An Optimized Segmentation Algorithm for the Surface Extraction in Computed Tomography for Metrology Applications [36]	2015	Spain	Canny, Deriche, Local Adaptive
A 3D edge detection technique for surface extraction in computed tomography for dimensional metrology applications [47]	2013	Spain	Canny, Local Adaptive

Table 2.2: List of papers of the literature review (1)

Region-based			
Title	**Year**	**Country**	**Method**
Investigation of Influence by Different Segmentation Parameters on Surface Accuracy in Industrial X-ray Computed Tomography [48]	2022	Serbia	Region Growing
Intelligent classification for three-dimensional metal powder particles [49]	2022	China	Watershed
Shape prior metal artefact reduction algorithm for industrial 3D cone beam CT [50]	2021	Korea	Chan-Vese based method
Watershed segmentation of topographical features on freeform surfaces and its application to additively manufactured surfaces [51]	2020	UK	Watershed
Improved surface extraction of multi-material components for single-source industrial X-ray computed tomography [52]	2020	Serbia	Region Growing
3D robust Chan-Vese model for industrial computed tomography volume data segmentation [53]	2013	China	Chan-Vese
Exploiting local intensity information in Chan-Vese model for noisy image segmentation [54]	2013	China	Chan-Vese
Quasi-optimal mesh segmentation via region growing/merging [55]	2007	Japan	Region-Growing
The application of volumetric region growing in segmentation for volume data from industrial computed tomography [56]	2005	China	Region-Growing
Visualizing Industrial CT Volume Data for Nondestructive Testing Applications [57]	2003	USA	Region-Growing
Seed-growing segmentation of 3-D surfaces from CT-contour data [58]	1999	Hong-Kong	Seed-Growing
Neural Networks			
Title	**Year**	**Country**	**Method**
Defect detection in CT scans of cast aluminum parts: A machine vision perspective [59]	2021	Germany	CNN
Development of a CNN edge detection model of noised X-ray images for enhanced performance of non-destructive testing [60]	2021	China	CNN
Analysis and experiment of effective factors in industrial CT dimensional measurement [25]	2021	China	Otsu, Phansalkar, FCM, MMPSO, NN
Industrial computerized tomography images segmentation based on cellular neural networks [61]	2011	China	CNN
Graph-based			
Title	**Year**	**Country**	**Method**
Identification of the number of overlapping welded thin plates in an X-ray CT volume [62]	2019	Japan	Multilabel Graph Cut
Generation of segmented triangular meshes from CT images based on centroidal Voronoi tessellation and the graph cut method [63]	2014	China	Graph-cut
Edge detection based multi-material interface extraction on industrial CT volumes [64]	2013	Japan	Multilabel Graph Cut
Clustering			
Title	**Year**	**Country**	**Method**
Analysis and experiment of effective factors in industrial CT dimensional measurement [25]	2021	China	Otsu, Phansalkar, FCM, MMPSO, NN
Detection and characterization method for interface bonding defects of new composite materials [65]	2019	China	FCM
Aluminum CT image defect detection based on segmentation and feature extraction [66]	2014	China	Clustering
Automated X-Ray Inspection of Aluminum Castings [67]	1988	Germany	Clustering

Table 2.3: List of papers of the literature review (2)

Miscellaneous			
Title	**Year**	**Country**	**Method**
Curvature Gradient-estimation Using CT Sinogram and its Application to Reverse Engineering [68]	2022	Japan	Morse Complex
An improved segmentation method for multi-material beam hardening correction in industrial x-ray computed tomography [69]	2019	USA	Joseph and Spital
SegMo: CT volume segmentation using a multi-level Morse complex [70]	2019	Japan	Morse complex
Markov random field segmentation for industrial computed tomography with metal artefacts [71]	2018	UK	MRF
A comprehensive method of contour extraction for industrial computed tomography images [72]	2013	China	Wavelet Transform
Fuzzy CT metrology: Dimensional measurements on uncertain data [73]	2013	Austria	Bayesian classification
Precise vectorization of industrial computed tomographic image [74]	2011	China	Facet model
Surface detection with subvoxel accuracy using facet model and IDDG operator [75]	2006	China	Facet model
Surface detection with subvoxel accuracy using 3-D directional derivatives [76]	1999	USA	Facet model

Reconstruction+Segmentation			
Title	**Year**	**Country**	**Method**
Fast binary CT using Fourier null space regularization (FNSR) [77]	2020	UK	Reconstruction+Segmentation
A 3D Bayesian Computed Tomography Reconstruction Algorithm with Gauss-Markov-Potts Prior Model and its Application to Real Data [78]	2017	France	Reconstruction+Segmentation
A promising limited angular computed tomography reconstruction via segmentation based regional enhancement and total variation minimization [79]	2016	China	Reconstruction+Segmentation

Table 2.4: List of papers of the literature review (3)

the image or volume being segmented.[80]

- **Boundary-based** methods, as the name suggests, focus on detecting the borders or boundaries between components based on the relative differences in grey values of voxels within a neighborhood. Unlike threshold-based methods that rely solely on intensity thresholds, boundary-based methods take into account the local variations in grey values to identify edges or boundaries. The advantage of boundary-based methods is their ability to capture local borders between components, which can be important in certain application scenarios. By considering the local variations, these methods can detect fine details and intricate structures within an image or volume.
- **Region-based** methods Region-based methods in segmentation involve the initialization of one or multiple regions, which are then expanded based on a homogeneity criterion. These methods aim to group pixels or voxels together into coherent regions that share similar characteristics. One example of a region-based method is region growing [81], which starts with seed regions. These seed regions can be manually set by the user or automatically determined by the algorithm. The algorithm then iteratively grows these seed regions by incorporating neighboring pixels or voxels that satisfy certain growing criteria. Another example of a region-based algorithm is the watershed transform [82]. In this method, regions are constructed by simulating a flooding process. The image or volume is considered as a topographic relief, and water is poured into the basins defined by the relief. As the water level rises, the basins start to merge, and the flooding process continues until a complete segmentation is obtained. Region-based methods are useful in scenarios where the boundaries between objects are not well-defined or when there are variations in the intensity or texture within regions.
- **Neural network** methods utilize neural networks for segmentation tasks. These methods leverage the capabilities of neural networks to learn and extract features from images, enabling accurate segmentation. Neural networks have shown promising results in various segmentation applications. One of the commonly used neural network architectures in image processing tasks, including XCT image analysis, is the Convolutional Neural Network (CNN). CNNs are particularly well-suited for tasks involving image recognition, classification, and segmentation.
- **Graph-based** methods utilize graph theory concepts to model and analyze the connectivity of image elements for segmentation purposes. These methods represent images as graphs, where nodes correspond to image elements, and edges

represent relationships between these elements. Graph-based algorithms exploit the connectivity information to achieve effective segmentation.

- **Clustering** methods involves the grouping of pixels or voxels into clusters based on their shared characteristics. Clustering methods typically utilize statistical techniques, such as k-means clustering, to model the underlying distribution of the data and assign pixels to the most suitable clusters. These algorithms prove particularly valuable when working with images that contain multiple objects or regions exhibiting diverse characteristics.
- **Miscellaneous** methods encompass segmentation approaches that primarily apply statistical and mathematical techniques. These methods may not fit into the previous macro classes but make valuable contributions to the segmentation field. They involve the utilization of statistical analysis, mathematical modeling, and other specialized techniques for segmentation purposes.

In addition to the identified classes of methods, it is worth noting that a distinct class emerged from the reviewed literature, which is referred as "Joint Reconstruction and Segmentation" in the Figure 2.2. This class encompasses methods that aim to integrate reconstruction and segmentation techniques together. These approaches aim to jointly address the challenges of accurate reconstruction and segmentation in computed tomography applications. While the number of papers specifically focusing on joint reconstruction and segmentation was limited, their inclusion highlights the growing interest in developing unified methodologies that can simultaneously address both reconstruction and segmentation tasks in the field of industrial computed tomography.

2.3. Current State of the Art of Segmentation

The conducted literature review focused on segmentation in X-ray Computed Tomography within an industrial context. Based on the analysis, specific algorithms emerged as the most frequently utilized within each macro class. For region-based algorithms, the Chan-Vese [83] and Region Growing methods were prominent in the selected papers. Global threshold-based algorithms commonly relied on the Otsu method [16], while boundary-based methods often employed the Canny algorithm [17]. Local adaptive threshold methods were identified as being widely applicable. Notably, Convolutional Neural Networks (CNN) methods were highly relevant in recent papers.

The analysis also revealed significant research activity in specific geographical regions. Spanish research groups primarily focused on edge-based algorithms such as Canny and

Deriche [18]. The Morse complex theory and graph-based methods received significant emphasis in Japanese research. Chinese groups showcased diverse topics, including Clustering, CNN, and Chan-Vese.

Regarding the objects used in the studies, no common objects were found across the examined papers. However, the most prevalent verification methods involved comparing the measurements obtained from the segmentation methods with established standards or commercial software, such as VGStudioMax, as well as with measurements obtained using Coordinate Measuring Machines (CMM). In some cases, the measurements were also compared to CAD models, predominantly in simulation-based works. These comparative evaluations were crucial for validating the performance of the segmentation methods.

In conclusion, the literature review conducted on segmentation in industrial computed tomography revealed valuable insights into the current state of the art. The main classes identified were threshold-based, boundary-based, region-based, neural network-based, graph-based, and miscellaneous methods. Each class encompasses specific techniques and approaches used for segmentation purposes.

The analysis highlighted the prevalence of certain algorithms within each macro class. Prominent methods included Otsu's method segmentation for global threshold-based techniques, the Canny edge detector for boundary-based methods, and region growing and Chan-Vese for region-based methods. Additionally, Convolutional Neural Networks (CNN) methods emerged as highly relevant in recent papers.

One notable limitation observed in the current state of the art is the lack of comprehensive and exhaustive comparisons among segmentation methods. Many studies focus on comparing algorithms to prove specific points rather than providing a clear general view or attempts at standardization. This limitation opens for future research to address the need for more extensive and standardized comparisons to guide the selection of segmentation methods.

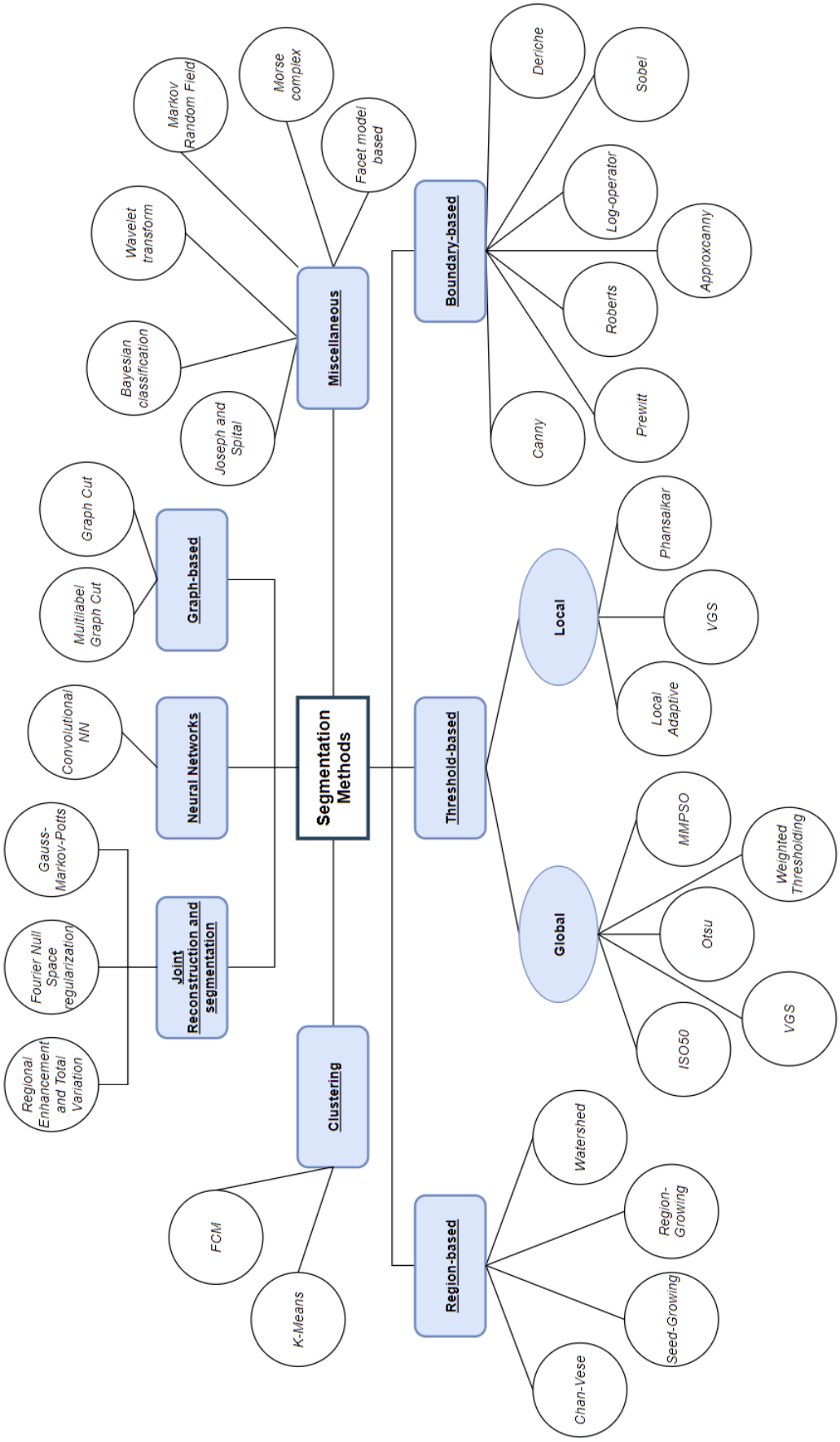

Figure 2.2: Map of the segmentation methods identified

3 | Experimental setup

The chapter is structured as follows. In Section 3.1, the XCT machine used in the study is described, along with the calibration process carried out prior to the actual scans. Section 3.2 provides details about the selected objects and the specific features chosen for evaluation. The software tools employed are outlined in Section 3.3. In Section 3.4, an overview of the selected segmentation methods is presented, including their formulation, implementation details, and the specific parameter settings used for each method. In 3.6, we describe the process of obtaining measurements for the selected features. Specifically, we explain how the point cloud obtained from the segmentation is processed.

3.1. XCT machine

X25 XCT scanner produced by North Star Imaging was utilized to scan the samples.

Figure 3.1: XCT scanner used

The tomographic system is composed of the following components:

- Manipulator controlled via software or through a hardware control console.
- X-ray generator produced by X-Ray Worx, model XWT-160-TC, using Tungsten as the target material.
- Flat detector produced by Dexela, model 1512N-C16-DRZS.
- Computers with dedicated software used for image acquisition and object reconstruction.

To mitigate the effects of beam hardening, an artifact caused by X-ray hardening, a physical filter was employed during the scan. Specifically, an aluminum filter was used for an aluminum sample.

Before conducting the scan, the system necessitates a warm-up phase, followed by a calibration phase for the geometry and sensor. The calibration and calibration phases are performed once the final position of the manipulator is determined. This involves analyzing a single scan of the sample to evaluate the optimal position.

The sensor calibration phase comprises two parts. The first part involves manual inspection of the pixels through a "blank" scan, allowing the detection and exclusion of any non-functioning pixels on the detector. The second part is an automatic correction process aimed at equalizing the response of the pixels. Three scans are carried out with different excitation currents (60 µA, 40 µA, and 20 µA), and a null current value, known as the "dark current," is assigned. Subsequently, the software performs the necessary corrections to equalize the pixel response.

The geometric calibration phase is conducted by scanning a sample provided by the scanner manufacturers (Figure 3.2). The sample consists of an aluminum base and a vertical column made of polymers containing equidistant calibrated tungsten spheres. During a 360° rotation of the turntable, the system performs a scan of the sample, recording the elliptical projection of the trajectories of the spheres on the detector. Geometric calibration of the system is then calculated based on the trajectories of the spheres. For the purpose of this automatic calibration, at least three spheres must remain within the acquisition window throughout the entire revolution.

Both calibration procedures need to be repeated at each warm-up cycle of the machine or whenever there is a change in the position of the manipulator.

Once the system calibration phases are completed, the scanning of the objects can be carried out.

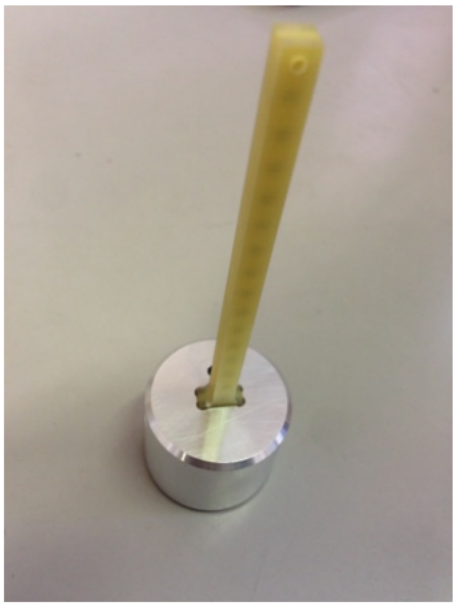

Figure 3.2: Sample used for XCT geometric calibration

3.2. Specimen and features evaluated

3.2.1. Specimen

The test sample used in the experiment was designed following the guidelines outlined in the German standard VDI/VDE 2630/2617, which is in accordance with the widely recognized ISO 10360 standard [84] for Coordinate Measuring Machine (CMM) systems. To create the sample, a lathe was employed, resulting in overlapping concentric cylinders as depicted in Figure 3.3.

The design specifications prescribed by the standard are as follows:

- The number of steps should be between 5 and 10.
- The ratio of height to diameter should range from 0.8 to 1.2.
- Linear diameter increments are used.
- The steps should be of equal size.
- The cylinders should be coaxial.

The maximum diameter chosen for the aluminum sample was 28 mm. As shown in Figure 3.3, there is a deviation from the standard regarding the height of the bottom step. In the sample, the height of the bottom step was set at 10mm. This decision was made to provide a region for gripping during the calibration using the CMM.

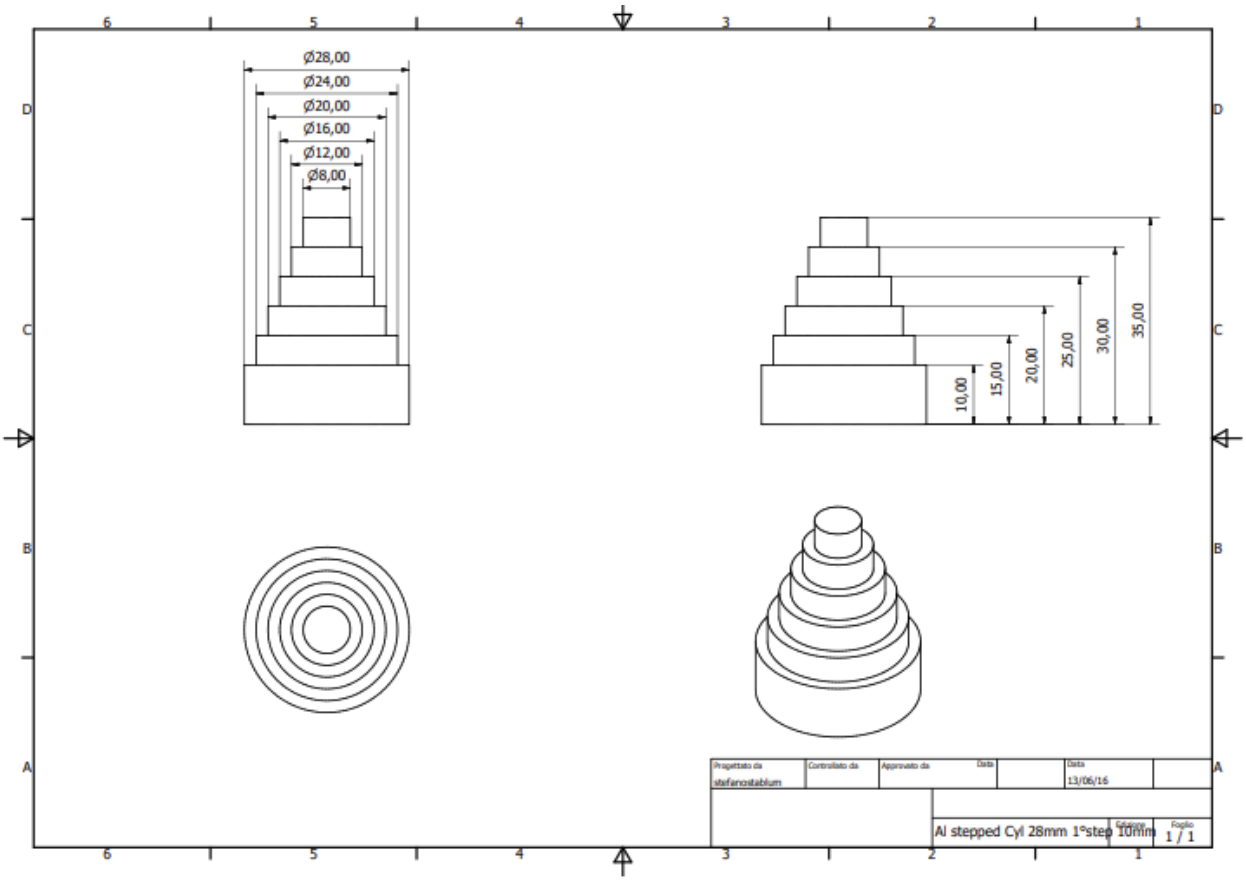

Figure 3.3: Technical drawing of the aluminum specimen

Table 3.1 provides an overview of the scan data obtained from the XCT machine. In total, there were 8 scans performed, each representing a distinct combination of two parameters: voltage and filter. The high voltage setting used in the scans was 90kV, while the lower voltage setting was 60kV. When the physical filter was employed, an aluminum filter with a thickness of 1.3mm was used. Other relevant parameter which were fixed in the different scans are:

- Voxel dimension: 0.0221 mm
- Number of projections: 1940
- Focal spot: 9.9 μm
- Frame averaging: 4
- Beam Hardening coefficient: 0.475

Additionally, four replicas were included for each parameter combination, resulting in a comprehensive dataset for analysis.

Parameter Combinations		
Scan	Filter	Voltage
TI1 and TI4	No	High
TI2 and TI6	No	Low
TI3 and TI7	Yes	Low
TI5 and TI8	Yes	High

Table 3.1: Choice of scans' parameters combination

Finally, Table 3.2 presents the measurements obtained from the calibration of the aluminum object using the CMM.

Results of the Calibrated Aluminum Object				
Geometrical feature	**Nominal value [mm]**	**Calibrated Value [mm]**	**Extended uncertainty**	**Coverage factor**
Diameter Cylinder 28	28	27.9795	0.2	2
Diameter Cylinder 24	24	23.9847	0.2	2
Diameter Cylinder 20	20	19.9886	0.2	2
Diameter Cylinder 16	16	15.9928	0.2	2
Diameter Cylinder 12	12	11.9942	0.3	2
Diameter Cylinder 8	8	7.9958	0.4	2
Cylindricity 8	N/A	0.0044	1.0	2
Cylindricity 12	N/A	0.0046	0.8	2
Cylindricity 16	N/A	0.0049	0.9	2
Cylindricity 20	N/A	0.0045	0.5	2
Cylindricity 24	N/A	0.0046	0.6	2
Cylindricity 28	N/A	0.0069	0.6	2
Cartesian Distance 5	5	4.9978	1.3	2
Cartesian Distance 10	5	4.9975	1.4	2
Cartesian Distance 15	5	4.9973	1.1	2
Cartesian Distance 20	5	4.9956	0.9	2
Cartesian Distance 25	5	4.9987	0.8	2

Table 3.2: Calibrated object measurement

3.2.2. Features

In our study, we aimed to measure and compare three various features of the specimens under investigation. More specifically, our focus was on assessing two features of size, namely the dimensional tolerance on the diameter (referred as "Diameter") and the dimensional tolerance on the distance between two planes (referred as "Height"). Additionally, the other one was related to the form tolerance, specifically the cylindricity

of the object (referred as "Cylindricity"). For the tolerance on the diameter, we solely considered the top step of the stepped cylinder, which had a fixed diameter of 8mm. Similarly, when evaluating the form tolerance, we concentrated solely on the top step to ensure consistency in the analysis. Lastly, we examined the tolerance on the distance between two planes considering all five steps of the stepped cylinder, enabling us to comprehensively assess any variations or deviations in the vertical dimension. By utilizing these specific feature extractions, we were able to conduct a comprehensive and precise analysis of the specimens under investigation.

3.3. Software processing

In order to perform the segmentation, MATLAB was utilized as the primary tool. However, prior to that, the data needed to be prepared for MATLAB analysis. This involved importing the NSI proprietary format file, obtained from the XCT machine, into VGStudio MAX [85], a software specifically designed for visualization and analysis of XCT data. Within VGStudio MAX, the data was subsequently exported as an *ANALYSE file*. This file format allowed for the creation of a suitable file that could be read by MATLAB as a volumetric matrix. The matrix contained the gray values of the object, in our case represented as *uint16* data format, facilitating the subsequent segmentation process.

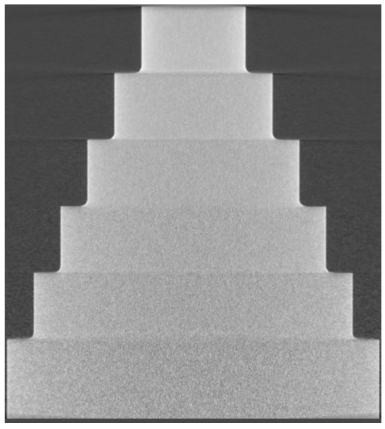

Figure 3.4: Raw grayscale image exported from VGStudioMax

3.4. Segmentation methods applied

This section introduces the segmentation methods employed in this study. Each method is presented along with its formulation. Subsequently, we describe how these methods

were implemented for our specific experiments, including the functions utilized and the parameter choices made.

3.4.1. Otsu

The Otsu's segmentation method was developed by Nobuyuki Otsu in 1979 [16] and has since become one of the most popular techniques for image segmentation.

It is a nonparametric and unsupervised method of automatic threshold selection. At its core, the Otsu method aims to find an optimal threshold value that separates an image into two classes: foreground and background. The goal is to set a discriminant criterion to evaluate the "goodness" of the threshold at the gray level k. One discriminat criterion that can be used from the discriminant analysis is

$$\eta = \frac{\sigma_B^2}{\sigma_T^2}$$

where σ_B^2 is the between-class variance and σ_W^2 is the within-class variance and they are computed as follow:

$$\sigma_B^2 = \omega_0\omega_1 \left(\mu_1 - \mu_0\right)^2$$

$$\sigma_W^2 = \omega_0\sigma_0^2 + \omega_1\sigma_1^2$$

being μ_0 and μ_1 the class mean level of the gray values of background and foreground respectively, and ω_0 and ω_1 the probabilities of class occurance.

Then the problem is reduced to an optimization problem to search for a threshold k that maximises the objective function η, so the optimal k^* that maximises η, or equivantely that maximises σ_B^2, can be obtain by

$$\sigma_B^2(k^*) = \underset{1\leq k<L}{max}\, \sigma_B^2(k)$$

The Otsu method's strength lies in its ability to automatically determine an optimal threshold without requiring prior knowledge about the image or manual parameter tuning. By maximizing the between-class variance, it effectively separates objects of interest from the background, making it particularly useful for image segmentation tasks.

For the implementation of the method, we utilized MATLAB functions:

$$T_{otsu} = graythresh(V)$$

to determine the Otsu's threshold value. V is the volumetric matrix containing the gray values.

3.4.2. Phansalkar

The Phansalkar method of segmentation is a technique used for local thresholding grayscale images. It was proposed by *N.Phansalkar et al.* [86] and provides an adaptive thresholding approach that can handle images with non-uniform illumination or varying contrast.

The Phansalkar method addresses the limitations of global thresholding techniques by considering local image characteristics. It calculates the threshold value for each pixel based on the statistical properties of its surrounding neighborhood.
To apply the Phansalkar method, the image is divided into overlapping windows or blocks, and for each block, a local threshold is computed. The size of the block and the level of overlap can be adjusted based on the characteristics of the image and the desired segmentation results.
The local threshold for each block is determined using the following formula:

$$T_{ph} = \mu \cdot \left(1 + k \cdot \left(\frac{\sigma}{R} - 1\right)\right)$$

Where μ and σ represent the average pixel intensity and the standard deviation within the block and they are computed as follows:

$$\mu = \frac{1}{N} \sum_{i=1}^{N} I(i,j)$$

$$\sigma = \sqrt{\frac{1}{N-1} \sum_{i=1}^{N} (I(i,j) - \mu)^2}$$

where N is the total number of pixels in the block and $I(i,j)$ is the intensity value of the pixel at position (i,j) in the image.

k and R are parameters that control the sensitivity of the thresholding. The value of

k determines the extent to which the threshold is influenced by the local standard deviation, while R helps normalize the standard deviation to a desired range.

After computing the local thresholds for each block, the Phansalkar method applies these thresholds to segment the image. Pixels with intensity values below the local threshold are assigned to the background, while pixels with intensity values above the threshold are considered part of the foreground.

The output of the Phansalkar method is a binary image where the foreground objects are separated from the background. By adapting the threshold based on local image characteristics, the Phansalkar method can effectively handle variations non-uniform illumination in the tomographic images.

For the implementation, since a 3D version of the methods was not available in MATLAB, we developed our own function based on the original paper and extended it to the third dimension. The script of the function can be found in the Appendix A. The function utilizes a cubic filter of dimensions *nxnxn* to iterate through the volumetric matrix and calculate the threshold value for each voxel based on the Phansalkar's formula discussed earlier.

To optimize the performance of the method for our specific case, we tuned the parameters: *p, q, R, k, n*.

The *R* parameter was set to 0.5 since the gray values of the volumetric matrix were rescaled between 0 and 1.

N.Phansalkar et al. [86] identified that the pixels corresponding to nuclei in the images lie below the value 0.4. Knowing that the exponential function in the formula reaches approximately 98% of its final value when the exponent is 4, then the relationship is set as follows:

$$q \cdot 0.4 = 4$$

Following the same logic, we computed its value based on the observation that, according to Otsu's method, the surface lies above its threshold value. Following the relationship presented above, we set the relationship for the *q* parameter as follows:

$$q \cdot T_{otsu} = 4$$

In the table below, the selected parameters for each scan are presented.

Phansalkar's parameters chosen					
Scan	**p**	**q**	**R**	**k**	**n**
TI1	15	9	0.5	0.25	5
TI2	15	9	0.5	0.25	5
TI3	15	6	0.5	0.25	5
TI4	15	9	0.5	0.25	5
TI5	15	8	0.5	0.25	5
TI6	15	8	0.5	0.25	5
TI7	15	9	0.5	0.25	5
TI8	15	9	0.5	0.25	5

Table 3.3: Selected parameters for Phansalkar segmentation

3.4.3. Canny

The Canny method of segmentation is an edge detection algorithm widely used in computer vision and image processing. It was developed by John Canny in 1986 and is known for its ability to accurately detect edges while minimizing noise and spurious responses.

At its core, the Canny method consists of several steps to achieve robust edge detection. These steps include:

Gaussian Smoothing: The input image is convolved with a Gaussian filter to reduce noise and create a smoothed representation of the image. This step helps to suppress high-frequency noise that can interfere with edge detection.

Gradient Calculation: The gradient of the smoothed image is computed using gradient operators such as the Sobel operator. The gradient magnitude $M(x, y)$ and direction $\theta(x, y)$ are determined for each pixel, representing the strength and orientation of the edges.

Non-maximum Suppression: Local maxima in the gradient magnitude are identified to obtain thin edges. This step involves suppressing non-maximum pixels along the direction perpendicular to the edge. Only pixels with the maximum gradient magnitude in their local neighborhood are preserved, while others are suppressed.

Double Thresholding: Two threshold values, a low threshold T_{low} and a high threshold T_{high}, are applied to classify the edges into strong, weak, and non-edges. Pixels with gradient magnitudes above the high threshold are considered strong edges, while those below the low threshold are classified as non-edges. Pixels with gradient magnitudes between the low and high thresholds are marked as weak edges.

Edge Tracking by Hysteresis: Weak edges that are connected to strong edges are retained, while isolated weak edges are discarded. This process involves connecting adjacent pixels that are part of the same edge and have a gradient magnitude above the low threshold.

The output of the Canny method is a binary image where the edges are detected as white pixels, while the non-edge regions are black. The algorithm effectively highlights the boundaries between different regions or objects in the image.

For Canny's implementation, we utilized the MATLAB function

$$edge3(V, approxcanny, [T_{low}, T_{high}])$$

This function applies the steps of the Canny method to detect edges in the volume V. It requires the selection of lower and higher thresholds for performing hysteresis thresholding. In our case, the table below presents the selected thresholds that yielded the best results.

Canny's parameters chosen		
Scan	T_{low}	T_{high}
TI1	0.15	0.5
TI2	0.15	0.5
TI3	0.15	0.5
TI4	0.15	0.5
TI5	0.15	0.5
TI6	0.10	0.2
TI7	0.05	0.2
TI8	0.15	0.5

Table 3.4: Selected parameters for Canny's thresholds

3.4.4. Chan-Vese

The Chan-Vese method of segmentation is a widely used algorithm for image segmentation. It was introduced by Tony F. Chan and Luminita A. Vese in 2001 [83] and is known for its ability to segment images into regions based on their intensity homogeneity.

At its core, the Chan-Vese method formulates segmentation as an energy minimization problem. It requires the definition of an initial contour, called Mask, that will iteratively evolve until it reaches the desired boundary. The method combines region-based and boundary-based techniques to achieve accurate segmentation.

The formulation of the Chan-Vese method involves the following steps:

- **Energy Functional**: The method defines an energy functional that represents the segmentation objective. It consists of two terms: the region term and the boundary term. The region term encourages homogeneity within each segmented region, while the boundary term promotes smoothness and regularity of the contour.
- **Minimization Process**: The energy functional is minimized iteratively using mathematical optimization techniques. This involves updating the contour to minimize the energy, while simultaneously adjusting the region parameters to improve the segmentation.

The Chan-Vese method often employs a level set formulation, where the contour is represented implicitly as the zero level set of a signed distance function. The level set framework allows for efficient evolution of the contour during the minimization process.

The output of the Chan-Vese method is a binary image where the segmented regions are represented as distinct regions separated by a contour. The contour separates the image into areas that exhibit homogeneous characteristics based on intensity values or other specified properties.

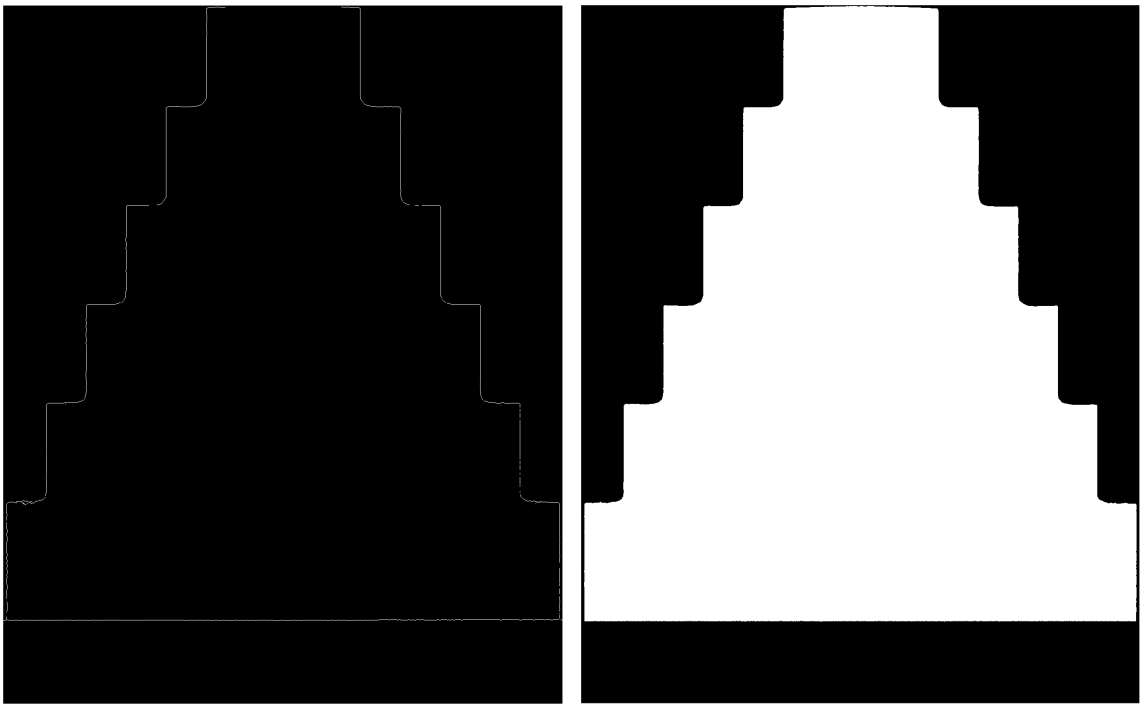

(a) Contour voxels identified by Canny. (b) Voxels identified by Chan-Vese.

Figure 3.5: Example of two segmentation results.

For the implementation of the segmentation method, we utilized the available MATLAB function

$$activecontour(V, Mask)$$

The *Mask* parameter represents the initial contour from which the segmentation evolution starts. It is specified as a binary image with the same size as the volumetric matrix.

Choosing a full-size binary matrix of ones as the initial mask would be the easiest option. However, due to the large size of the volumetric matrix, this choice would render the computation infeasible. Therefore, a smaller and simpler mask was selected. In this case, a square-based parallelepiped with dimensions slighlty smaller than the object is being used as the initial mask.

3.4.5. VGStudioMax

In addition to the methods, it is also been considered the measurements of the features from the surface determination result of the software VGStudioMax. For this software, different evaluation methods have been considered.

- **Direct measurement from software**: the results have been calculated directly using the tools available on the software for the evaluation of the features
- **Exporting the representation of the surface determination**: the result coming from the surface determination has been exported as a *mesh* using three different representations available on the software. The differences are presented in the Table 3.5

VGStudio Surface Determination Representations	
Name	**Description**
Grid-based	Applies a conversion algorithm that is suitable for working with full resolution and yields high-quality meshes.
Ray-based	Applies a conversion algorithm that is suitable for working with reduced resolution.
Grid-based + Simplification	Same as the Grid-based. The simplification algorithm combines groups of triangles to larger triangles, reducing reducing the overvall number (Figure 3.6)

Table 3.5: Different representations of the surface determination used

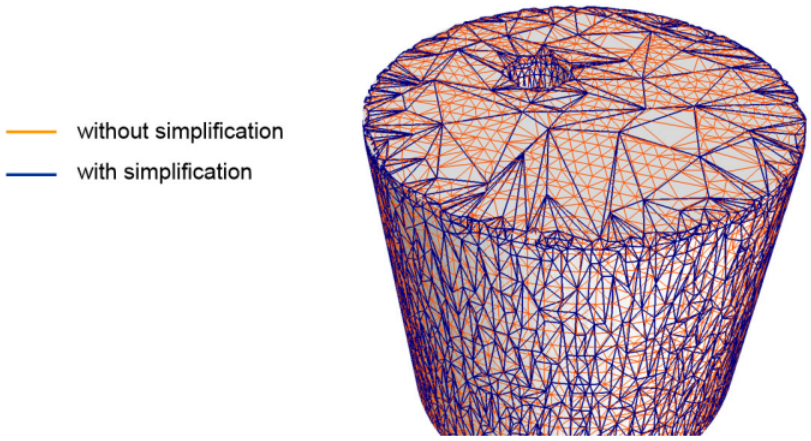

Figure 3.6: Example of the simplification algorithm performed by VGStudio software [85]

3.5. Canny + Subvoxel

As we already presented in Section 1.4, subvoxeling techniques allows a more precise estimation of the position of the surface of an object with subvoxel accuracy, going beyond the limitations of discrete voxel grid coordinates.

The decision to apply the subvoxeling technique to the Canny method was driven by its ability to directly identify the voxels corresponding to the surface, eliminating the need for an additional step to determine surface points. Furthermore, considering that a significant portion of the research contributions in boundary-based methods came from a particular research group that mainly utilized the Canny and Deriche methods, we chose to replicate their subvoxeling technique applied to Canny to enable a comparison with a state-of-the-art method.

3.5.1. Explanation of the literature subvoxeling technique

Following the initial surface voxel identification using the Canny algorithm, a gravity center algorithm is employed to enhance the spatial resolution of the edge. This algorithm is applied to a neighborhood, referred to as a window, around each of the local maximum points detected by Canny. The optimal window size is 3 (Figure 3.7), which means considering only the closest neighboring voxel for the calculation.

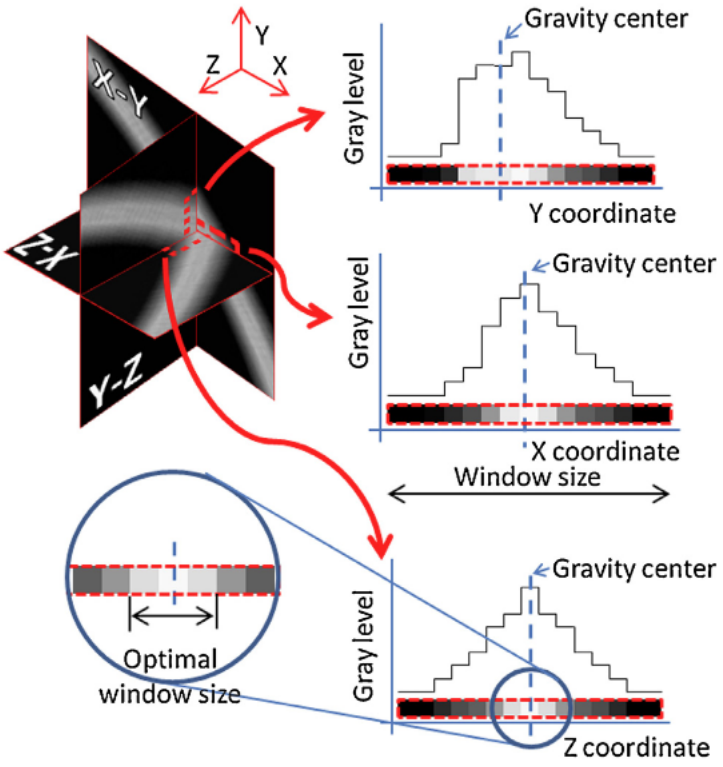

Figure 3.7: Application of the Gravity center algorithm to the three directions [47]

The optimal positions of the points inside the voxel are calculated by applying:

$$X' = \frac{\sum_{i=1}^{i=3}(X_i \cdot G_{X,i})}{\sum_{i=1}^{i=3}(G_{X,i})}; Y' = \frac{\sum_{j=1}^{j=3}(Y_j \cdot G_{Y,j})}{\sum_{j=1}^{j=3}(G_{Y,j})}; Z' = \frac{\sum_{k=1}^{k=3}(Z_k \cdot G_{Z,k})}{\sum_{k=1}^{k=3}(G_{Z,k})};$$

where X', Y' and Z' are the optimal positions of the points in the x-,y- and z-axis. X_i, Y_j and Z_k are the coordinates of the voxels inside the window, and i, j and k indicate the number of the voxel, i.e from 1 to 3 for the window considered. $G_{X,i}, G_{Y,j}$ and $G_{Z,k}$ are the gray value transitions obtained in the preliminary surface detection for the X, Y and Z directions.

The refinement has been carried out separately and independently along all the three directions. This technique is described in detail in the study by Yagüe-Fabra et al. (2013) [47].

3.5.2. Formulation of subvoxeling technique

In this work, we used the Taylor expansion series to identify the subvoxel accurate locations of the edge which corresponds to the zero-crossings in the second derivative

of the grey values in the gradient direction. We attempted to adapt and apply a method commonly used in image processing to our XCT grayscale volumes, aiming to combine it with the results obtained from the Canny algorithm. This approach allowed us to explore the potential application of this method in the context of XCT data analysis.

The formulation of Taylor expansion series is as follows:

In a local neighborhood of point **a**, the function f can be approximated along a line in the gradient direction using a third-order Taylor polynomial [87]. The third-order Taylor polynomial is given by:

$$f\left(\mathbf{a}+w\hat{\mathbf{w}}\right) \approx f\left(\mathbf{a}\right)+wf_{w}\left(\mathbf{a}\right)+\frac{1}{2}w^{2}f_{ww}\left(\mathbf{a}\right)+\frac{1}{6}w^{6}f_{www}\left(\mathbf{a}\right)$$

In this equation, $f\left(\mathbf{a}\right)$ represents the value of f at point **a**, $f_{w}\left(\mathbf{a}\right)$ denotes the first derivative of f at point **a** along the gradient direction, $f_{ww}\left(\mathbf{a}\right)$ represents the second derivative and $f_{www}\left(\mathbf{a}\right)$ represents the third derivative, and w represents the coordinate along the line. The grey values along this line are given by

$$g\left(w\right)=f\left(\mathbf{a}+w\hat{\mathbf{w}}\right)$$

The zero crossing in the second-order derivative can be determined as follows:

$$g''\left(w\right)=f_{ww}+wf_{www}\left(\mathbf{a}\right)$$

Therefore, the zero crossing relative to **a** can be found at:

$$\mathbf{a}_{zc}=\mathbf{a}-\frac{f_{ww}\left(\mathbf{a}\right)}{f_{www}\left(\mathbf{a}\right)}\hat{\mathbf{w}}$$

To compute the derivatives on the data, we used the MATLAB function *imgradientxyz*, which returns the directional gradients along the x, y and z directions of the three-dimensional greyscale volume.

We first applied a Gaussian smoothing filter on the data and subsequently we applied the function *imgradientxyz* to compute the matrices of first derivates in x, y and z. Applying again the same functions to the three new matrices, we are able to obtain the second derivatives terms: *xx*, *yy*, *zz*, *xy*, *xz*, *yz*. Finally, the function is applied one last time on the obtained terms to obtain the third derivative terms: *xxx*, *yyy*, *zzz*, *xxy*, *xyy*, *xxz*, *xzz*, *yyz*, *yzz*, *xyz*.

With these terms we are now able to define the second and third derivatives in three-dimensions as follows:

$$f_{ww} = f_x^2 f_{xx} + f_y^2 f_{yy} + f_z^2 f_{zz} + 2f_x f_y f_{xy} + 2f_x f_z f_{xz} + 2f_z f_y f_{zy}$$
$$f_{www} = f_x^3 f_{xxx} + f_y^3 f_{yyy} + f_z^3 f_{zzz} + 3f_x^2 f_y f_{xxy} + 3f_x f_y^2 f_{xyy} + 3f_x^2 f_z f_{xxz} + 3f_x f_z^2 f_{xzz}$$
$$+3f_z^2 f_y f_{zzy} + 3f_z f_y^2 f_{zyy} + 3f_z f_y f_z f_{xyz}$$

So, the new point's coordinates will be:

- **x** = $a_x - \frac{f_{ww}}{f_{www}} \cdot f_x$
- **y** = $a_y - \frac{f_{ww}}{f_{www}} \cdot f_y$
- **z** = $a_z - \frac{f_{ww}}{f_{www}} \cdot f_z$

Where a_x, a_y, and a_z represent the coordinates in the x, y, and z directions of the original point identified by Canny. On the other hand, f_x, f_y, and f_z correspond to the partial derivatives of f with respect to x, y, and z, respectively. These derivatives represent the gradients in the x, y, and z directions of the image.

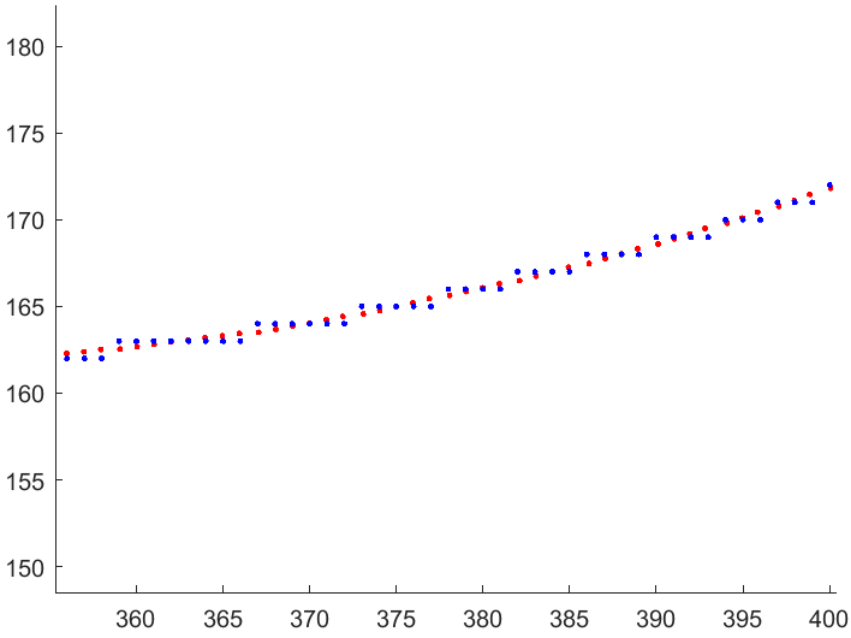

Figure 3.8: Subvoxel refinement compared to the initial identified points by Canny

Figure 3.8 provides a visual representation of the subvoxel refinement technique applied

to the Canny segmentation method. The blue points represent the centroids of the edge voxels identified by Canny, while the red points represent the new points generated after displacement through the subvoxel refinement technique.

The blue points exhibit a saw-tooth configuration, which is characteristic of using voxel centroids for edge detection. This configuration can introduce some irregularities in the contour. In contrast, the red points, which have been moved along the gradient direction using the subvoxel refinement technique, form a smoother and more continuous contour. This displacement of points allows for a more accurate representation of the object's boundary.

3.6. Surface definition and measuring methods

In our feature extraction and measurement procedure, we utilized the segmented volume obtained from various segmentation algorithms. In the case of Phansalkar and Chan-vese, the algorithms provided a binary map indicating the location of the object. To generate a surface from these binary maps, we used the MATLAB function $isosurface(binarymatrix, isovalue)$ with an isovalue of 0.5. This returned the vertices of the polygon surface, which were then used for measurements.

For the algorithms that directly provided the surface points, such as Canny and its subvoxel implementation, we simply extracted the coordinates of these points. For the Otsu method, we employed the function $isosurface(binarymatrix, T_{otsu})$ to generate the surface at the determined isovalue. This approach was chosen because Otsu's threshold inherently provides the value of the surface, enabling a subvoxel implementation of the method.

Once we obtained the vertices of the surface, we employed specific functions to extract the diameter, cylindricity, and height. For diameter and cylindricity measurements, we utilized the $ctollbyfervs$ function (Appendix A), which calculate the cylindricity tolerance of a set of points using the Carr-Ferreira algorithm, which reduces the original non-linear problem to a sequence of linear problems that converge to the solution of the problem. The function requires the vector X containing the x, y and z coordinates of the surface points. The function returns two outputs: the cylindricity tolerance and the mean radius of the cylinder.

To perform height measurements, we conducted a more extensive data preparation process. We extracted the point clouds of all planes and the bottom step of the cylinder. To calculate the five height of the stepped cylinder, we utilized the $planeDist$ function

(Appendix A). This function incorporates the $lscylinder$ function, which employs the Gauss-Newton algorithm to fit a circle that provides an estimated point on the axis of the stepped cylinder. Subsequently, the point clouds of the planes were fitted, and the distance between two planes was computed as the distance between two points on the axis, each belonging to one of the two planes.

4 | Results

In this chapter, we present the results obtained from the measurements of the three selected features: diameter, cylindricity, and height. The measurements serve as a means to evaluate the accuracy and precision of the XCT process compared to the calibrated measurements obtained from the CMM (Coordinate Measuring Machine).

Additionally, we provide insightful observations on the relationships between the chosen criteria.

The measurements are reported and visualized through a series of plots, where the deviations from the calibrated measurements are depicted on the coordinate axis. The abscissa axis represents the different criteria used to evaluate the segmentation, including the segmentation methods employed, the presence or absence of a physical filter, and the application of high or low voltage. Each data point on the plot represents the mean of all related measurements, providing a representative indication of the overall performance.

By analyzing the results, we gain valuable insights into the accuracy and reliability of the segmentation methods applied. Furthermore, we assess the impact of varying parameters such as the presence of a physical filter and the voltage settings. These findings contribute to a comprehensive understanding of the segmentation process and provide valuable information for further optimization and improvement of the XCT technique.

All the observations have been validated through the analysis of the variance (ANOVA), in order to provide a statistical evidence of the observations and to further understand and quantify the dependencies of the results on the different factors.

Overall, this chapter offers a comprehensive overview of the obtained results, highlighting the deviations in measurements and providing significant observations regarding the segmentation criteria.

In the table below are listed the methods used with their abbreviation and a summary of the surface representation algorithm used.

Methods used and corresponding surface representation		
Method	**Abbreviation**	**Surface representation**
Otsu	Otsu	Marching Cube
Canny	Canny	None
Canny Subvoxel	CannySV	Taylor Expansion Series
Canny from literature	Canny[47]	Gravity Center Algorithm
Phansalkar	PH	Marching Cube
Chan-Vese	CV	Marching Cube
Direct measurement in VGStudio	VGS	VGStudio software
Grid-based representation of VGStudio	VGS(grid)	VGStudio software
Grid-based representation of VGStudio + simplification	VGS(grid+s)	VGStudio software
Ray-based representation of VGStudio	VGS(ray)	VGStudio software

Table 4.1: Table of methods and their surface representation

It is important to note that the analysis of the diameter and cylindricity included a comprehensive comparison among all the methods. However, for the height measurement, there were some issues with reproducibility, which led to a separate analysis of the Cann[47] method. This separate analysis involved comparing Canny[47] to the other methods using only four tomographic images, without their respective replicas. Although this limited analysis provided a visual understanding of the algorithm's performance compared to our implementation based on the available data at our disposal.

4.1. Diameter

Based on the analysis of the results, it is evident that the different segmentation methods exhibit distinct behaviors, as shown in Figure 4.1. The Chan-Vese and Phansalkar methods tend to overestimate the diameter with values between 15 and 18 µm, while Otsu and the commercial software VGStudioMax tend to underestimate it with values between -16 and -19 µm. Notably, the Canny edge detector and the two subvoxel implementations stand out with a significantly lower measurement deviation compared to Otsu and VGStudioMax, with deviations of only -4.5 and -4 µm respectively. Both subvoxel refinements technique does not exhibit a significant improvement compared to the Canny segmentation method. The measurements only show a slight improvement, suggesting that the impact of subvoxel refinement on diameter estimation is limited.

Another interesting finding is related to the three different surface determination representations provided by VGStudioMax. Despite the differences in representation, the resulting measurements were highly similar.

The presence of a physical filter was observed to contribute to measurement underestimation, with a reduction in underestimation of approximately 72% from a deviation of -11 to -3 µm when the filter was absent. This suggests that the physical filter introduces additional factors that affect measurement accuracy for this particular feature. Furthermore, higher voltage settings were found to result in more accurate measurements.

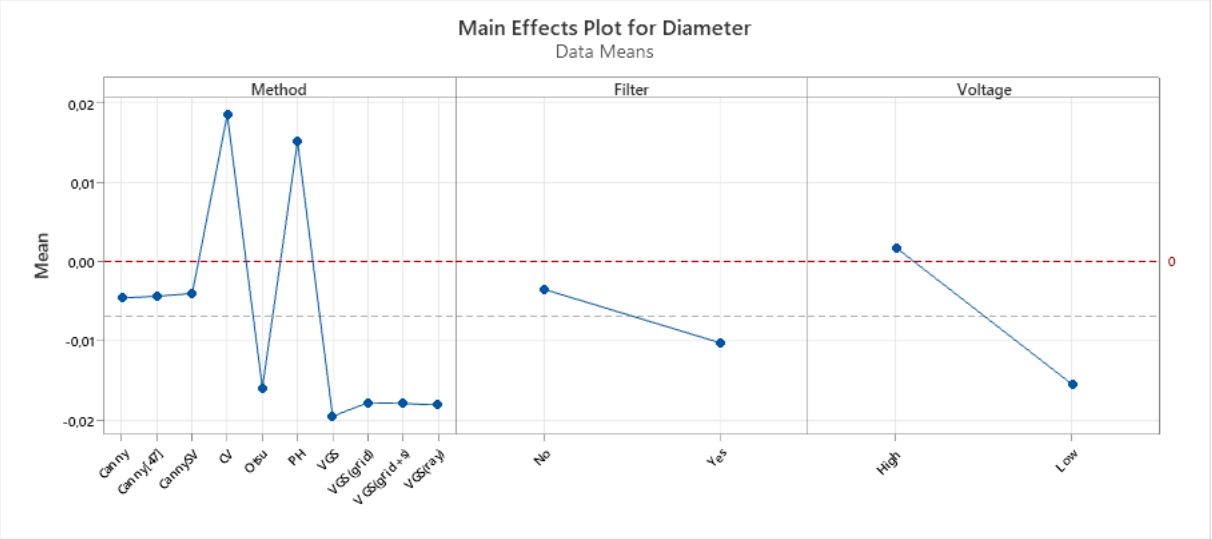

Figure 4.1: Main effects plot for the results of the diameter [mm]

Figure 4.2 illustrates the interaction between various parameters in the segmentation process. One notable relationship explored is the interaction between the segmentation method and the presence of a physical filter. It is evident that certain methods are affected by the presence or absence of the filter in terms of diameter measurements. Otsu, Chan-Vese, and Phansalkar methods tend to underestimate measurements when the filter is present, while VGStudioMax, Canny, Canny subvoxel and Canny[47] methods appear to be unaffected by the filter.

Another influential factor is the voltage level used in the XCT scans. Comparing measurements obtained at low and high voltage settings, it is observed that lower voltage levels tend to result in underestimation of measurements across all segmentation methods. This emphasizes the importance of voltage settings in achieving accurate segmentation outcomes.

Furthermore, when considering the relationship between voltage and the presence of the filter, it is clear that the impact of the filter on measurements is relatively minor compared to the influence of voltage. The presence of the filter does not significantly affect the measurements, whereas voltage levels have a substantial effect. Measurements obtained at low voltage exhibit more pronounced underestimation compared to those

obtained at high voltage.

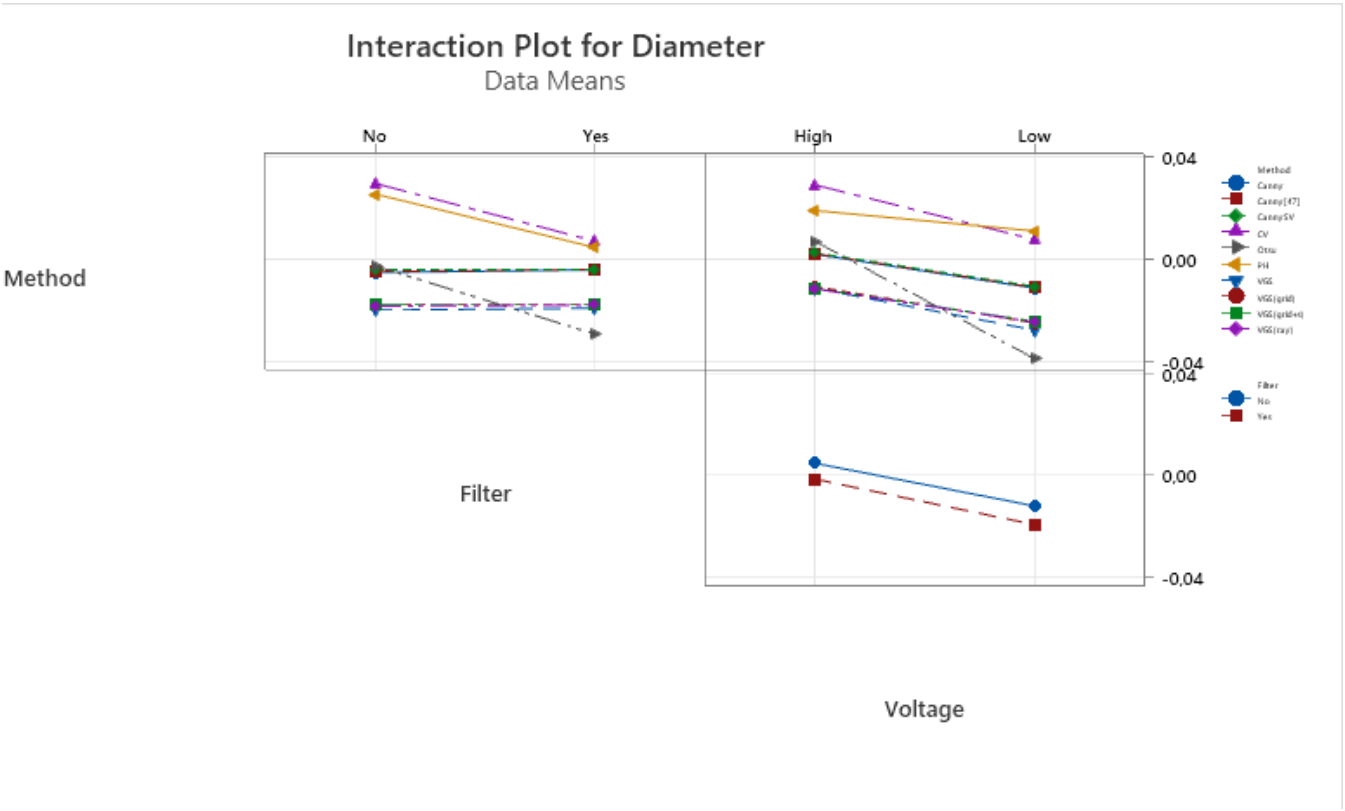

Figure 4.2: Interaction plot for the results of the diameter [mm]

In Figure 4.3, focusing on the measurement of the diameter, there is an interesting aspect to explore regarding the relationship between the segmentation method and the specific Tomographic Image (TI) on which the method is applied. Although Figure 4.1 draws the same conclusion regarding the overall performance, indicating that the three Canny methods and Otsu methods generally produce more accurate results, a closer examination uncovers an interesting observation. In the third volume, it is evident that the Otsu method significantly underestimates the diameter compared to both its average performance and the measurements obtained by other methods.

This discrepancy could potentially be attributed to the influence of noise present in the tomographic image or a stronger influence of the beam hardening artifact, as well as the robustness of the Otsu method in addressing such issues.

This finding emphasizes the importance of considering the specific characteristics of tomographic images when selecting the appropriate segmentation method. While the Canny and Otsu methods generally demonstrate strong performance, it is crucial to acknowledge their potential vulnerability to certain image characteristics and take necessary precautions to mitigate any adverse effects.

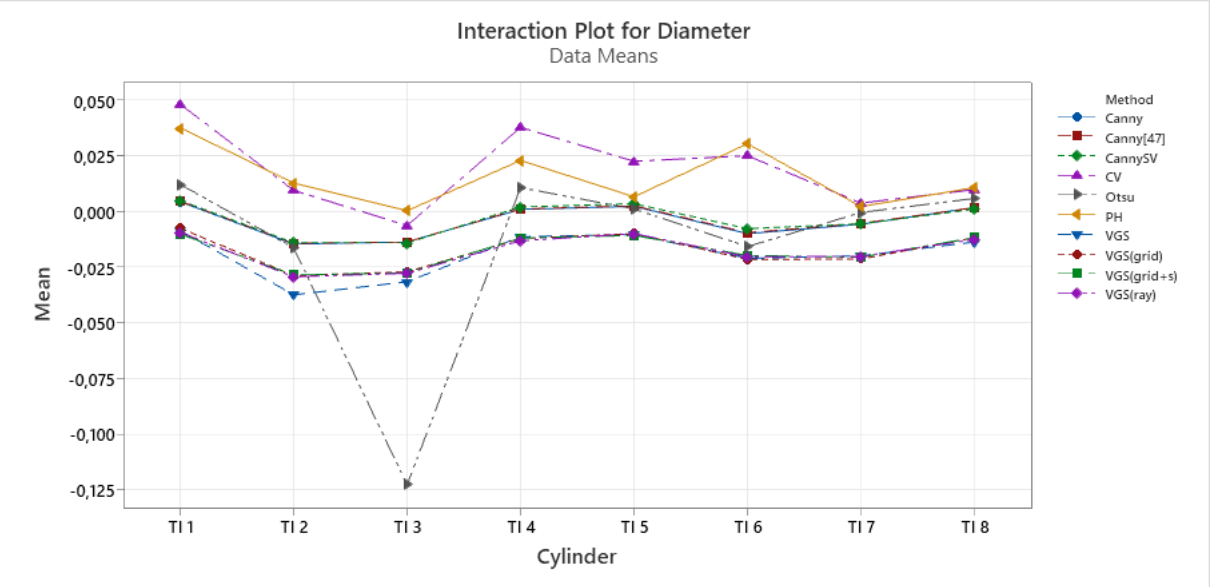

Figure 4.3: Effects of the segmentation method with respect to each tomographic image (diameter) [mm]

In conclusion, the results obtained from the analysis of the segmentation methods provide valuable insights into their behavior and performance. The Canny edge detector, especially its subvoxel implementations, emerges as a favorable choice, exhibiting superior measurement accuracy compared to other methods. Furthermore, the influence of factors such as physical filters and voltage settings on measurement accuracy has been highlighted. The absence of a physical filter and the use of higher voltage settings have shown to contribute to improved measurement accuracy.

To provide statistical evidence and support the observations, Figure 4.4 presents the analysis of variance (ANOVA) results for the diameter. In order for the test to be considered valid, a standard 5% significance level was applied to the 3 factors under consideration and their interactions.

The ANOVA results indicate that both the Method and the Voltage have a significant impact on the measurement, as evidenced by the respective p-values. In particular, the Voltage factor shows a substantial difference in the magnitude of the F-value compared to the other factors.

Contrary to the initial visual observations from the plots, the Filter factor seems to have a very limited impact on the measurement result, as indicated by its p-value, which is approximately 4,6%.

Additionally, none of the interactions between factors demonstrate any significant

influence on the measurement.

Analysis of Variance

Source	DF	Adj SS	Adj MS	F-Value	P-Value
Method	9	0,014074	0,001564	7,24	0,000
Filter	1	0,000913	0,000913	4,23	0,046
Voltage	1	0,005959	0,005959	27,59	0,000
Method*Filter	9	0,002427	0,000270	1,25	0,294
Method*Voltage	9	0,002074	0,000230	1,07	0,407
Filter*Voltage	1	0,000006	0,000006	0,03	0,871
Method*Filter*Voltage	9	0,000767	0,000085	0,39	0,931
Error	40	0,008638	0,000216		
Total	79	0,034857			

Figure 4.4: ANOVA - Diameter

4.2. Cylindricity

In Figure 4.5, an interesting observation can be made regarding the measurement of cylindricity and its comparison to the calibrated measurement of the CMM. The results show that methods such as Canny, Chan-Vese, and Phansalkar tend to significantly overestimate the cylindricity compared to the CMM measurement. On the other hand, Otsu and the direct measurement on VGStudio software yield more accurate results. Canny instead demonstrates a notable improvement with our subvoxel refinement but not from Canny[47] technique, which instead performs just slightly better than the original Otsu. In the CannySV the deviation from the CMM measurement is reduced by approximately 20 micrometers, indicating a more precise estimation of cylindricity. Canny with subvoxeling significantly improves also the accuracy of cylindricity measurement compared to the standard methods, bringing it to 9.5 µm. The deviations from the calibrated measurement of the CMM are notably reduced, indicating a higher level of precision. Furthermore, it is interesting to note that the subvoxel refinement technique surpasses the performance of the other two best-performing techniques, namely Otsu and the direct measurement on VGStudio, respectively at 15.3 and 13.8 µm. This improvement highlights the effectiveness of the subvoxel refinement approach in achieving more accurate and reliable cylindricity measurements. The comparison provides strong evidence for the superiority of the subvoxel refinement technique, positioning it as a highly promising method for cylindricity measurement in the context of X-ray Computed Tomography.

Additionally, it is noteworthy that the different representations of the same surface deter-

mination in VGStudio behave differently. The representation with the highest number of points considered on the surface (grid-based representation without simplification) performs overall worse in terms of cylindricity measurement. This discrepancy could be attributed to the number of points generated by these representations, indicating that a higher density of points does not necessarily result in better cylindricity measurement, but can instead lead to a higher risk of incurring in outlying points.

Interestingly, the presence or absence of the filter does not seem to have a significant impact on the cylindricity measurement. Unlike the diameter measurement, higher voltage tends to underestimate the measurement compared to the lower voltage, but in the case of cylindricity, this also provides better results.

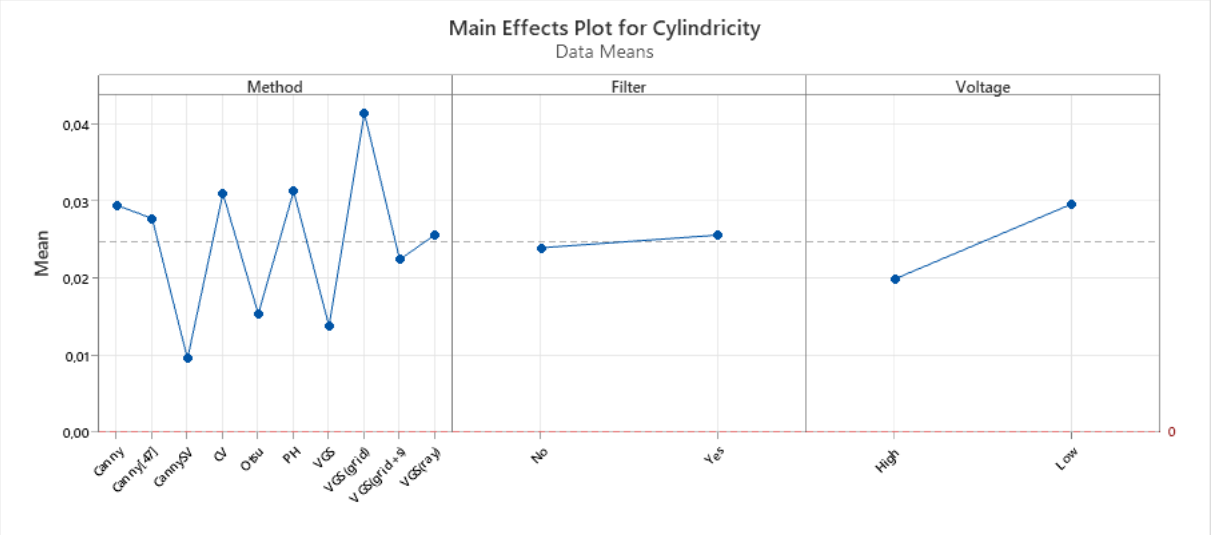

Figure 4.5: Main effects plot for the results of the cylindricity [mm]

In the interaction plot for cylindricity in Figure 4.6, the influence of the method and the presence of the filter can be observed. Most of the methods, such as Phansalkar, Chan-Vese, Canny, and direct measurement in VGStudio, are not significantly affected by the presence of the filter. These methods demonstrate consistent performance regardless of the filter.

However, there are two distinct behaviors observed in the Otsu method and the ray-based and grid-based representations in VGStudio. In the Otsu method and the grid-based representation, the absence of the filter leads to better results in terms of cylindricity measurement. On the other hand, in the ray-based VGStudio representation, the filter improves the measurement accuracy.

Regarding the voltage setting, it is evident that all methods benefit from higher voltage. Increasing the voltage contributes to an improved accuracy in cylindricity measurement

across the different methods. This observation underlines the importance of voltage settings in obtaining more reliable and precise measurements.

In the remaining comparisons, it is further evident that voltage plays a more significant role compared to the filter. Additionally, the presence of the filter appears to have a more pronounced effect at higher voltage settings.

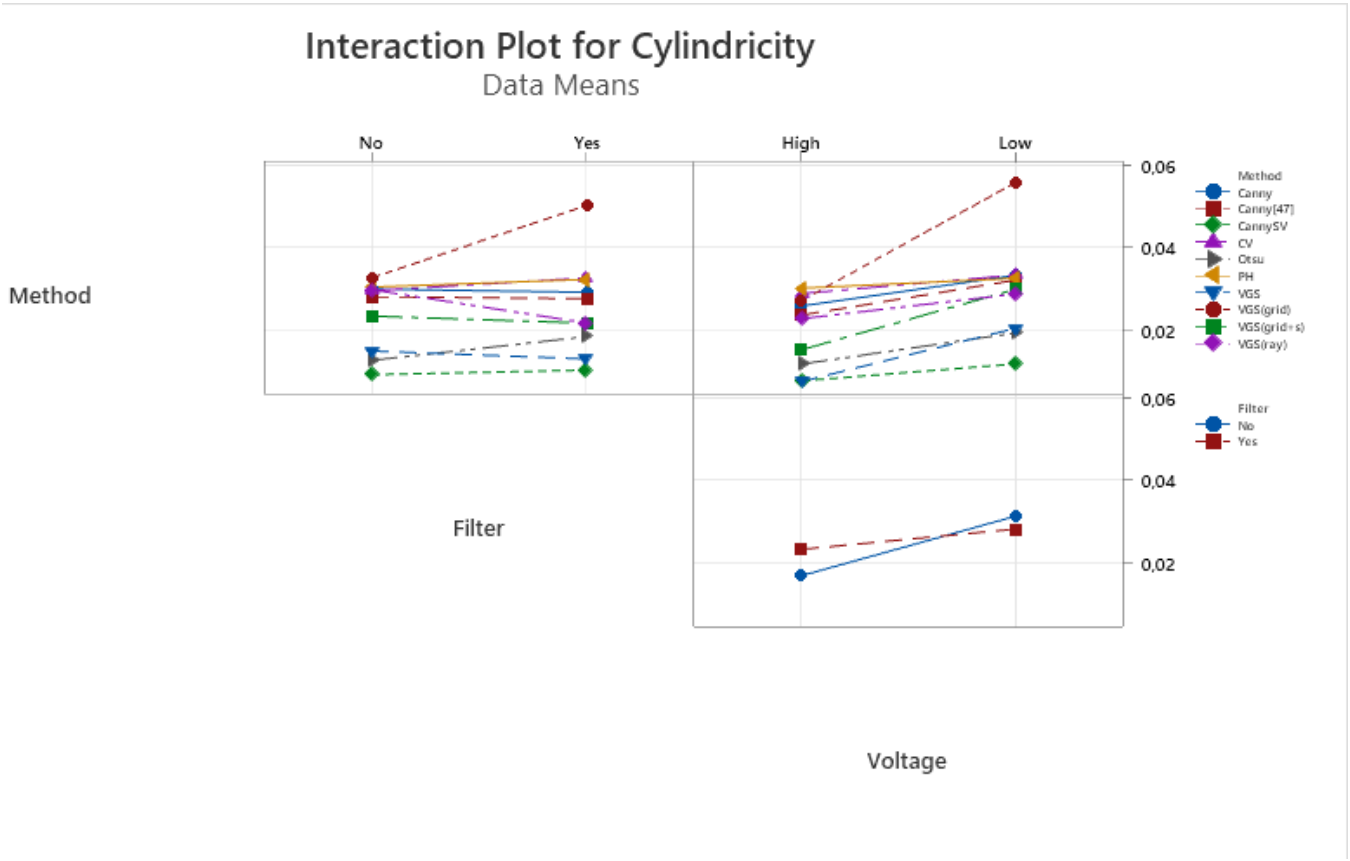

Figure 4.6: Interaction plot for the results of the cylindricity [mm]

In Figure 4.7 a comparison of the methods with the tomographic images is presented. It is observed that most methods exhibit similar performance, while a few stand out in terms of their accuracy in cylindricity measurement. The direct measurement on the commercial software and the Otsu method are notable for their performance, but CannySV seems to be superior in all the different scans.

The direct measurement on the software proves to be the most accurate in terms of cylindricity measurement. However, it is interesting to note that two representations of the surface determination in the software perform particularly good as well, while the third representation (grid-based) consistently yields poor results across the tomographic images. This discrepancy suggests that the choice of the representation within the

software can significantly impact the accuracy of the measurement.

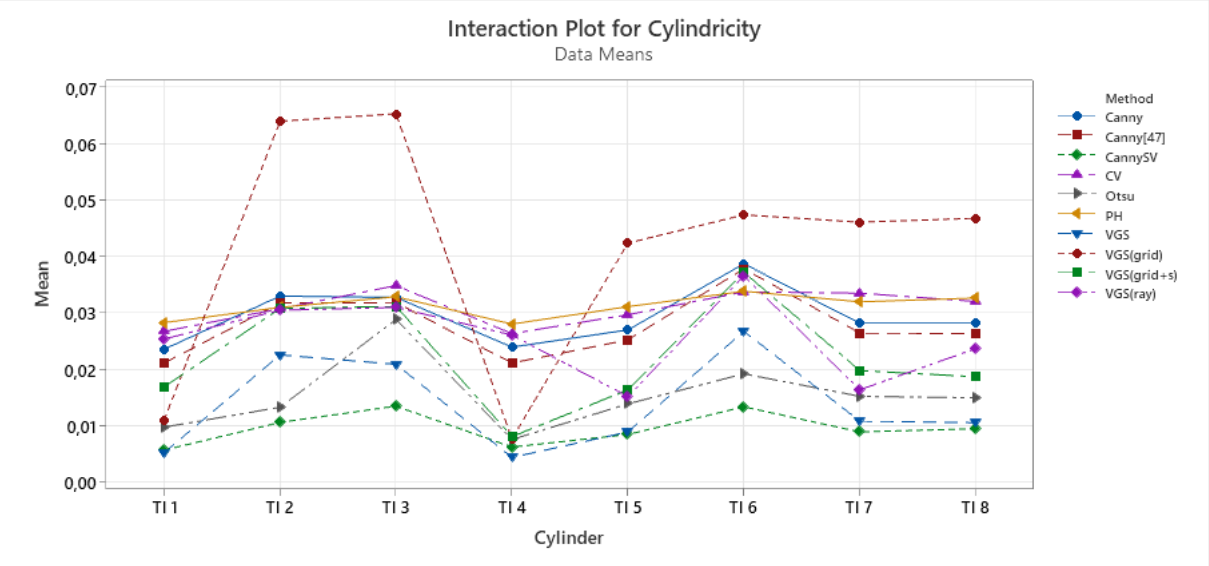

Figure 4.7: Effects of the segmentation method with respect to each tomographic image (cylindricity) [mm]

Again, to provide statistical evidence for the observations made from the plots, an analysis of variance (ANOVA) was conducted. The results further support the findings.

The ANOVA results in Figure 4.8 indicate that both the Method and Voltage factors have a significant impact on the measurement, as indicated by the p-values. The Voltage factor has a particularly high F-value, suggesting a stronger influence on the measurement compared to other factors.

Similar to previous findings, the Filter factor does not show any significant influence on the measurement, as evidenced by its p-value.

However, the interactions between factors reveal significant influences on the measurement. Specifically, the Method-Filter, Method-Voltage, and Filter-Voltage interactions exhibit statistical significance. Among these interactions, the Filter-Voltage interaction stands out as particularly influential. As observed in the interaction plot, the behavior of the filter changes at high or low voltages. Notably, the absence of the filter at high voltage yields better results compared to having the filter, while the presence of the filter is worse at low voltages.

On the other hand, the Method-Filter-Voltage interaction does not demonstrate any relevance or significant influence on the measurement.

Analysis of Variance

Source	DF	Adj SS	Adj MS	F-Value	P-Value
Method	9	0,006661	0,000740	33,26	0,000
Filter	1	0,000054	0,000054	2,44	0,126
Voltage	1	0,001886	0,001886	84,75	0,000
Method*Filter	9	0,000808	0,000090	4,04	0,001
Method*Voltage	9	0,001067	0,000119	5,33	0,000
Filter*Voltage	1	0,000456	0,000456	20,49	0,000
Method*Filter*Voltage	9	0,000470	0,000052	2,35	0,031
Error	40	0,000890	0,000022		
Total	79	0,012293			

Figure 4.8: ANOVA - Cylindricity

4.3. Height

In the analysis of the height feature in Figure 4.9, it is observed that the standard methods perform similarly, with the Canny method showing slightly better results with a deviation of 7.8 µm and the Phansalkar method performing slightly worse at 12.2 µm. On the other hand, the measurements obtained from VGStudioMax appear to be the best. Notably, the measurements from the representations in VGStudioMax tend to approach the 0 value, even outperforming the direct measurement on the software. However, it is important to consider that this could be the result of an overestimating systematic error in the measurement. Another important observation is that the Canny with subvoxel shows a significant deterioration in the measurement, with an underestimation of approximately -20 µm. This discrepancy may be attributed to the incorrect identification of certain points on the planes. Furthermore, it was observed that the top and bottom planes posed the greatest difficulty in being accurately identified.

Examining the results in terms of each step, an interesting observation emerges. The first three steps from the bottom tend to overestimate the measurement of the height feature, while the last two steps tend to underestimate it. This pattern could potentially be attributed to a cone beam artifact. Due to the cone beam shape of the X-rays, when they hit areas far from the middle of the object, a positive and negative cupping effect may occur. This effect could contribute to the observed overestimation and underestimation of the height measurement.

Furthermore, the presence of the filter and the voltage level appear to have less impact on the height measurement. However, it is worth noting that the presence of the filter and a lower voltage level may yield slightly better results.

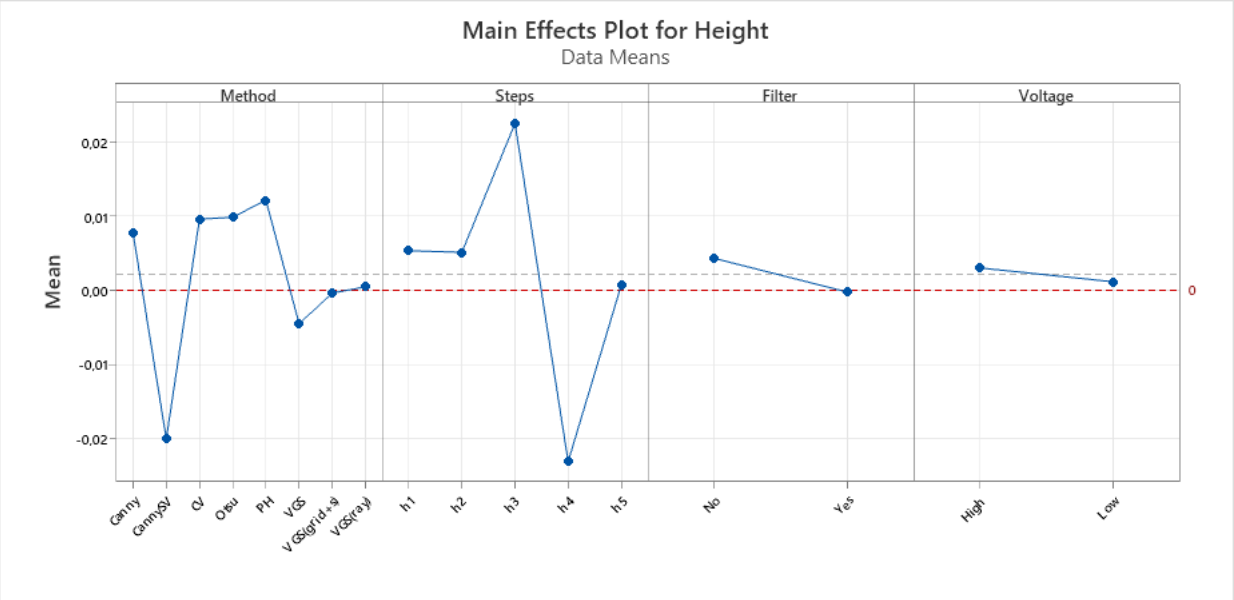

Figure 4.9: Main effects plot for the results of the height [mm]

To gain further insights into the plot, we conducted ANOVA analysis. The results of the ANOVA (Figure 4.10) reaffirm that the step measured has a significant influence on the measurement, as indicated by its small p-value. On the other hand, the analysis suggests that the other factors do not have a notable impact on the measurement. Although, examining the second order factors, the combination of the method and filter has a significant impact on the measurement. This is evident from the p-value of zero, indicating the relevance of the method in relation to the specific step being considered. In other words, the choice of method becomes influential depending on the particular step of the object.

Although some results are missing, it is still interesting to compare the results obtained for the height when analyzing only four tomographic images using the Canny[47] subvoxeling technique (Figure 4.11). This method shows very similar results to our Canny subvoxeling technique, with the measurement heavily underestimating compared to the original Canny.

Moreover, when considering the different steps, it becomes evident that the top step (h1) is the most influenced by the addition of this other subvoxeling method, resulting in a more significant underestimation. On the other hand, the bottom step (h5) obtains an overestimation compared to the results displayed in Figure 4.9. These findings may indicate that the subvoxeling accuracy is influenced by the type of dimensional tolerance being considered.

Analysis of Variance

Source	DF	Adj SS	Adj MS	F-Value	P-Value
Method	7	0,03524	0,005034	1,81	0,089
Steps	4	0,06360	0,015899	5,71	0,000
Filter	1	0,00304	0,003045	1,09	0,297
Voltage	1	0,00107	0,001074	0,39	0,535
Method*Steps	28	0,38333	0,013690	4,92	0,000
Method*Filter	7	0,00009	0,000013	0,00	1,000
Method*Voltage	7	0,00030	0,000043	0,02	1,000
Steps*Filter	4	0,02571	0,006429	2,31	0,060
Steps*Voltage	4	0,01706	0,004264	1,53	0,196
Filter*Voltage	1	0,00213	0,002131	0,77	0,383
Method*Steps*Filter	28	0,00924	0,000330	0,12	1,000
Method*Steps*Voltage	28	0,01137	0,000406	0,15	1,000
Method*Filter*Voltage	7	0,02861	0,004086	1,47	0,183
Steps*Filter*Voltage	4	0,03566	0,008915	3,20	0,015
Method*Steps*Filter*Voltage	28	0,37389	0,013353	4,80	0,000
Error	150	0,41738	0,002783		
Total	309	1,25003			

Figure 4.10: ANOVA - Height

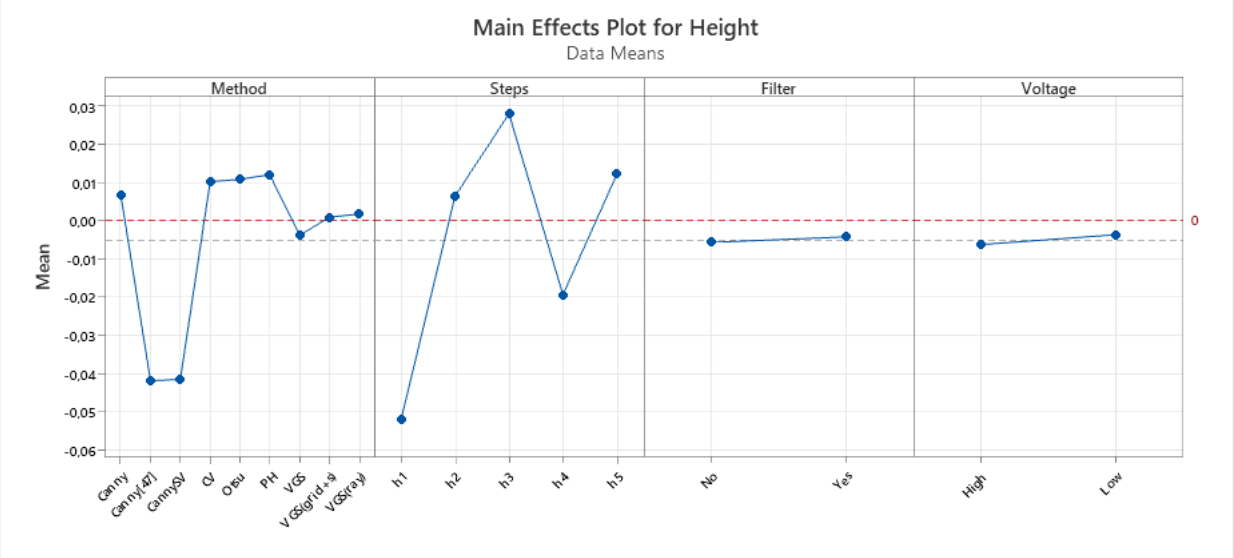

Figure 4.11: Main effects plot for the results of the height with Canny[47] [mm]

4.4. Discussion

In summary, the comparison of segmentation methods on the three distinct features revealed interesting findings. Canny proved to be highly effective for diameter measurements, surpassing even the subvoxeling methods like Otsu and direct measurements from VGStudio. Although Canny performed better than standard methods for the other features, it couldn't match the accuracy of subvoxeling techniques. This discrepancy can be attributed to the discrete nature of surface points identified by standard segmentation methods, limiting their precision, especially in the cylindricity. For height measurements, Canny displayed potential by outperforming standard methods, although not being the best overall. Recognizing this potential, the decision was made to implement a subvoxeling refinement of the Canny algorithm.

The introduction of Canny Subvoxel brought remarkable improvements in the cylindricity measurements. However, it did not yield substantial improvements in diameter measurements and it did encounter difficulties in accurately identifying some points for height measurements, resulting in a significant impact on the overall results. This is likely due the increased noise in the flat surfaces, which are almost parallel to the X-rays. Based on the observation from the ANOVA analysis for the height measurement, where the method's relevance is evident in its interaction with the step, it suggests that the choice of methods is task-specific. This means that different methods may perform better or worse depending on the specific characteristics of the object or feature being measured.

It is also worth looking at the probability plots for the residuals in the three cases (Figure 4.15).

The diameter measurements exhibit a relatively aligned distribution of points along a line, with the exception of two outliers. Despite these outliers, the overall result is considered satisfactory as the model used for analysis is balanced [88], ensuring an equal number of observations for each level or combination of levels in the ANOVA. In the case of cylindricity, the points form a S-shaped configuration, closely following the reference line. This indicates a good approximation of the true cylindricity, reinforcing the accuracy of the measurements. The height measurements display a similar behavior to the diameter, with the points showing a tendency to align along a line. However, the presence of multiple outlier points introduces variability and affects the alignment of the overall distribution along the reference line.

When comparing the results with the Canny method from the literature, it showed very

similar measurements of the diameter compared to the other Canny methods applied in this work. However, our Canny with subvoxeling outperformed both methods in the measurement of cylindricity. On the other hand, both subvoxeling techniques performed poorly in the height measurement compared to the original Canny and the other methods.

These observations are further supported by conducting a pairwise comparison of the methods using Bonferroni's method to assess the similarity among the segmentation techniques.

Grouping Information Using the Bonferroni Method and 95% Confidence

Method	N	Mean	Grouping	
CV	8	0,0185330	A	
PH	8	0,0151972	A	
CannySV	8	-0,0039963	A	B
Canny[47]	8	-0,0043499	A	B
Canny	8	-0,0045676	A	B
Otsu	8	-0,0159160		B
VGS(grid)	8	-0,0177750		B
VGS(grid+s)	8	-0,0178750		B
VGS(ray)	8	-0,0180750		B
VGS	8	-0,0195038		B

Means that do not share a letter are significantly different.

Figure 4.12: Comparisons for the diameter

As shown in Figure 4.12, the methods have been divided into two main groups. Being part of the same group indicates similarity in performance compared to the other methods in the same group. For the diameter, the three Canny methods are grouped together and belong to both groups.

On the other hand, when looking at cylindricity (Figure 4.13), more groups are identified. In this case, Canny and Canny[47] belong to the same group but show dissimilarity with CannySV, which is instead grouped together with the other two methods that apply a subvoxeling technique, namely Otsu and direct measurement using VGStudio software.

Finally, when examining the comparison for the height and excluding Canny[47], as we can see from Figure 4.14 the methods do not display significant differences in performance from each other and are grouped together. However, the ANOVA (Fig. 4.10) shows that the interaction between methods and heights is significant. The pairwise comparison is not reported here, as it is difficult to interpret.

Grouping Information Using the Bonferroni Method and 95% Confidence

Method	N	Mean	Grouping			
VGS(grid)	8	0,0413375	A			
PH	8	0,0312321		B		
CV	8	0,0309716		B		
Canny	8	0,0294293		B	C	
Canny[47]	8	0,0277185		B	C	
VGS(ray)	8	0,0256125		B	C	
VGS(grid+s)	8	0,0223875			C	D
Otsu	8	0,0153577				D	E
VGS	8	0,0137804					E
CannySV	8	0,0095440					E

Means that do not share a letter are significantly different.

Figure 4.13: Comparisons for the cylindricity

Grouping Information Using the Bonferroni Method and 95% Confidence

Method	N	Mean	Grouping
PH	40	0,0122072	A
Otsu	40	0,0099397	A
CV	40	0,0096716	A
Canny	35	0,0070974	A
VGS(ray)	40	0,0005550	A
VGS(grid+s)	40	-0,0003000	A
VGS	40	-0,0044157	A
CannySV	35	-0,0250658	A

Means that do not share a letter are significantly different.

Figure 4.14: Comparisons for the height

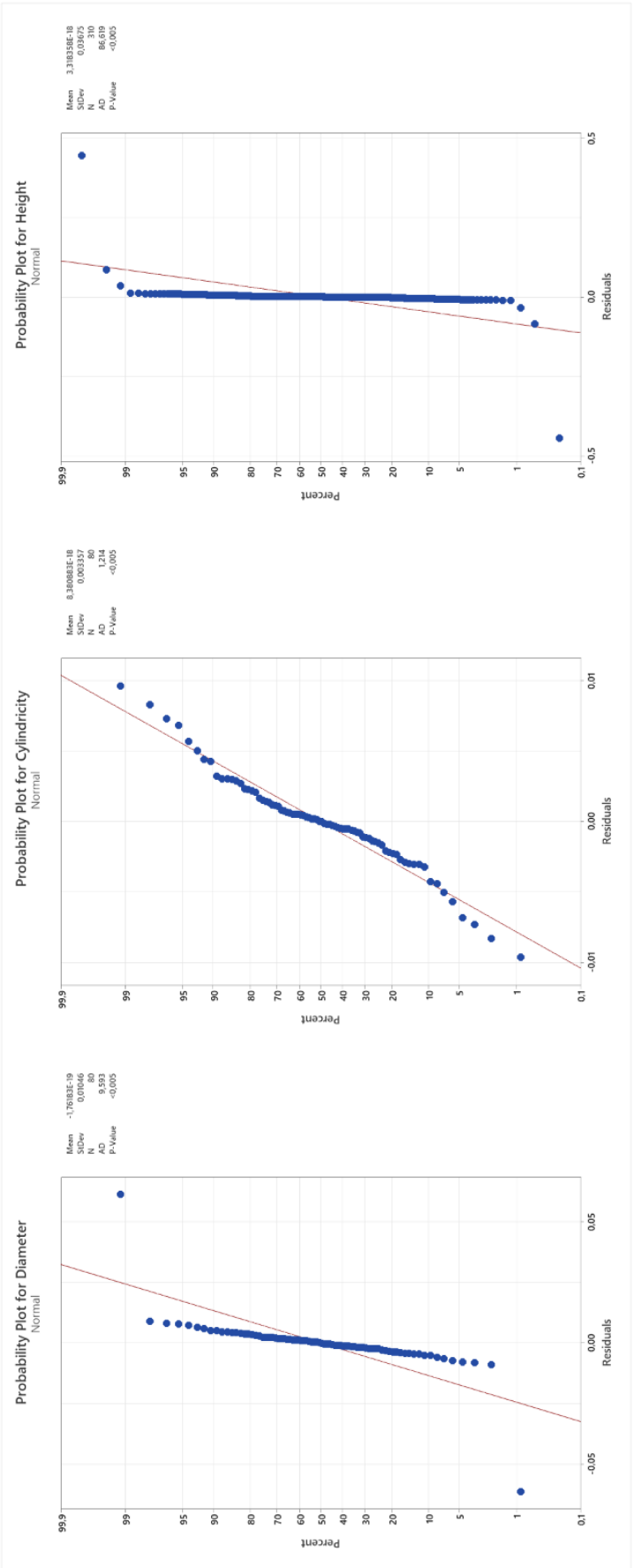

Figure 4.15: Probability plots of the residuals for the three features

5 | Concluding remarks and outlook

This thesis aimed to overcome the limitations in segmentation analysis found in existing literature, specifically in industrial computed tomography. The ability of XCT to capture detailed information about complex-shaped parts, which conventional measuring systems often struggle to provide, makes it a valuable tool for quality control and dimensional analysis. However, the XCT process is not without challenges, and one crucial aspect is the segmentation process.

A thorough research of the current state of the art on segmentation in industrial XCT was conducted, resulting in a comprehensive review. This review encompassed seven major categories of segmentation methods, revealing the prevalent approaches used in industrial XCT segmentation.

To address the aforementioned lack of comparison among algorithms specified for different measurands, a comparative analysis of segmentation methods was carried out. This analysis focused on three key features: diameter, cylindricity, and height. To facilitate this evaluation, an aluminum stepped cylinder was introduced as a standardized test object. The results revealed that no single method performed optimally for all features and conditions. Different methods exhibited strengths and weaknesses depending on specific requirements, emphasizing the importance of considering objectives, features, and scanning conditions when selecting segmentation methods for industrial XCT applications.

Additionally, a subvoxeling technique was proposed in this thesis to enhance the measurement accuracy of segmentation methods at a subvoxel level. By leveraging Taylor Expansion series up to the third order, this technique aimed to improve surface detection. The evaluations of the subvoxeling technique revealed the following performances:

- Consistent with results obtained with the origina Canny method on the feature of size of the diameter.
- Excellent for the form tolerance on the cylinders, surpassing other methods and those that inherently incorporate subvoxeling.

- Poor performance for the feature of size related to the height.

Overall, this thesis contributes to the advancement of segmentation analysis in industrial XCT by providing insights into the strengths and weaknesses of different segmentation methodologies across various features. The comprehensive literature review, comparative evaluations, and the proposed subvoxeling technique address the current limitations and highlight the challenges and opportunities in the field.

The findings underscore the need for more extensive and standardized comparisons among segmentation methods. Clear guidelines and benchmarks are necessary to aid researchers and industrial users in selecting the most appropriate algorithms. Further research should explore the application of the subvoxeling technique to other features and objects to validate its generalizability and investigate potential improvements.

Bibliography

[1] G. N. Hounsfield, "Computerized transverse axial scanning (tomography): Part 1. description of system," *The British journal of radiology*, vol. 46, no. 552, pp. 1016–1022, 1973.

[2] W. A. Kalender, "X-ray computed tomography," *Physics in Medicine & Biology*, vol. 51, no. 13, p. R29, 2006.

[3] P. Reimers *et al.*, "New possibilities of nondestructive evaluation by x-ray computed tomography," 1983.

[4] H. Wiacker, "Dimensionsanalyse mit der computertomografie am beispiel turbinenschaufel vermessung. 2," in *Seminar Computertomografie, DGZfP BB*, vol. 22, pp. 86–93, 1991.

[5] J. P. Kruth, M. Bartscher, S. Carmignato, R. Schmitt, L. De Chiffre, and A. Weckenmann, "Computed tomography for dimensional metrology," *CIRP annals*, vol. 60, no. 2, pp. 821–842, 2011.

[6] E. Ametova, G. Probst, and W. Dewulf, "X-ray computed tomography devices and their components," *Industrial x-ray computed tomography*, pp. 69–98, 2018.

[7] W. Sun, S. Brown, and R. Leach, "An overview of industrial x-ray computed tomography.," 2012.

[8] J. L. Ball, A. D. Moore, and S. Turner, *Ball and Moore's essential physics for radiographers*. John Wiley & Sons, 2012.

[9] U. Ewert, "New trends in industrial radiology," *Journal of Nondestructive Testing*, vol. 7, no. 2, 2002.

[10] J. Jing, S. Liu, G. Wang, W. Zhang, and C. Sun, "Recent advances on image edge detection: A comprehensive review," *Neurocomputing*, 2022.

[11] S. Carmignato, W. Dewulf, and R. Leach, *Industrial X-ray computed tomography*, vol. 10. Springer, 2018.

[12] G. Moroni and S. Petrò, "Impact of the threshold on the performance verification of computerized tomography scanners," *Procedia Cirp*, vol. 43, pp. 345–350, 2016.

[13] J. Lifton, A. Malcolm, and J. McBride, "On the uncertainty of surface determination in x-ray computed tomography for dimensional metrology," *Measurement Science and Technology*, vol. 26, no. 3, p. 035003, 2015.

[14] T. Tóth, A. Végh, M. Dovica, and J. Živčák, "Influences of surface determination for measurements obtained by industrial computed tomography," in *Applied Mechanics and Materials*, vol. 683, pp. 142–146, Trans Tech Publ, 2014.

[15] C. Heinzl, J. Kastner, B. Georgi, and H. Lettenbauer, "Comparison of surface detection methods to evaluate cone beam computed tomography data for three dimensional metrology," in *Proc. of the International Symposium on Digital industrial Radiology and Computed Tomography*, Citeseer, 2007.

[16] N. Otsu, "A threshold selection method from gray-level histograms," *IEEE transactions on systems, man, and cybernetics*, vol. 9, no. 1, pp. 62–66, 1979.

[17] J. Canny, "A computational approach to edge detection," *IEEE Transactions on pattern analysis and machine intelligence*, no. 6, pp. 679–698, 1986.

[18] R. Deriche, "Using canny's criteria to derive a recursively implemented optimal edge detector," *International journal of computer vision*, vol. 1, no. 2, pp. 167–187, 1987.

[19] H. Villarraga-Gómez, E. L. Herazo, and S. T. Smith, "X-ray computed tomography: from medical imaging to dimensional metrology," *Precision Engineering*, vol. 60, pp. 544–569, 2019.

[20] J. Hiller and P. Hornberger, "Measurement accuracy in x-ray computed tomography metrology: Toward a systematic analysis of interference effects in tomographic imaging," *Precision Engineering*, vol. 45, pp. 18–32, 2016.

[21] B. S. Institution, "Part 1: Non-destructive testing - radiation methods for computed tomography," 2019.

[22] H. Villarraga-Gómez, *Studies of dimensional metrology with X-ray CAT scan*. PhD thesis, The University of North Carolina at Charlotte, 2018.

[23] Y. nan Wang, S. san Shuai, X. fu Ren, T. tong Hu, J. Wang, and Z. ming Ren, "Sub-pixel high precision dimensional measurement method for aero-engine hollow

turbine blade based on industrial computed tomography image," *China Foundry*, vol. 19, pp. 307–320, 7 2022.

[24] J. Großeheide, K. Geiger, A. Schmidt, C. Bütow, B. Montavon, and R. H. Schmitt, "Adaptive surface geometry determination in multi-material x-ray computed tomography using fringe projection," *Measurement Science and Technology*, vol. 33, 4 2022.

[25] X. Li, E. Shang, H. Yu, M. Teng, F. Yang, and K. Huang, "Analysis and experiment of effective factors in industrial ct dimensional measurement," in *2021 6th International Conference on Communication, Image and Signal Processing (CCISP)*, pp. 219–223, IEEE, 2021.

[26] W. Shen, X. Zhang, X. Jiang, L. H. Yeh, Z. Zhang, Q. Li, B. Li, and H. Qin, "Surface extraction from micro-computed tomography data for additive manufacturing," vol. 53, pp. 568–575, Elsevier B.V., 2021.

[27] Y. Quinsat, J. B. Guyon, and C. Lartigue, "Qualification of ct data for areal surface texture analysis," *The International Journal of Advanced Manufacturing Technology*, vol. 100, pp. 3025–3035, 2019.

[28] A. Townsend, R. Racasan, R. Leach, N. Senin, A. Thompson, A. Ramsey, D. Bate, P. Woolliams, S. Brown, and L. Blunt, "An interlaboratory comparison of x-ray computed tomography measurement for texture and dimensional characterisation of additively manufactured parts," *Additive Manufacturing*, vol. 23, pp. 422–432, 10 2018.

[29] M. Torralba, R. Jiménez, J. A. Yagüe-Fabra, S. Ontiveros, and G. Tosello, "Comparison of surface extraction techniques performance in computed tomography for 3d complex micro-geometry dimensional measurements," *International Journal of Advanced Manufacturing Technology*, vol. 97, pp. 441–453, 7 2018.

[30] J. Zheng, D. Zhang, K. Huang, and Y. Sun, "A cbct series slice image segmentation method," *Journal of X-Ray Science and Technology*, vol. 26, no. 5, pp. 815–832, 2018.

[31] T. Kowaluk and A. Wozniak, "A new threshold selection method for x-ray computed tomography for dimensional metrology," *Precision Engineering*, vol. 50, pp. 449–454, 10 2017.

[32] A. Townsend, L. Pagani, P. Scott, and L. Blunt, "Areal surface texture data extraction from x-ray computed tomography reconstructions of metal additively manufactured parts," *Precision Engineering*, vol. 48, pp. 254–264, 4 2017.

[33] J. Liu, "Precision evaluation of the reconstruction model based on unigraphics," in *2017 10th International Symposium on Computational Intelligence and Design (ISCID)*, vol. 1, pp. 358–361, IEEE, 2017.

[34] A. Kraemer and G. Lanza, "Assessment of the measurement procedure for dimensional metrology with x-ray computed tomography," vol. 43, pp. 362–367, Elsevier B.V., 2016.

[35] A. Stolfi, M. K. Thompson, L. Carli, and L. D. Chiffre, "Quantifying the contribution of post-processing in computed tomography measurement uncertainty," vol. 43, pp. 297–302, Elsevier B.V., 2016.

[36] R. Jiménez, C. Comps, and J. Yagüe, "An optimized segmentation algorithm for the surface extraction in computed tomography for metrology applications," *Procedia engineering*, vol. 132, pp. 804–810, 2015.

[37] F. Welkenhuyzen, D. Indesteege, B. Boeckmans, K. Kiekens, Y. Tan, W. Dewulf, and J.-P. Kruth, "Accuracy study of a 450 kv ct system with a calibrated test object," 2013.

[38] J. Li, L. Wang, J. Wei, and H. Wen, "An image segmentation algorithm based on kernel estimation and moment-preserving," vol. 2, 2010.

[39] J. Li, L. Zhou, H. Yu, H. Liang, and L. Zhang, "Classification for volume rendering of industrial ct based on minimum cross entropy," 2007.

[40] J. Li, "Classification for volume rendering of industrial ct based on moment of histogram," 2007.

[41] C. Heinzl, J. Kastner, E. Gröller, and G. Gröller, "Surface extraction from multi-material components for metrology using dual energy ct," 2007.

[42] A. F. Obrist, A. Flisch, and J. Hofmann, "Point cloud reconstruction with sub-pixel accuracy by slice-adaptive thresholding of x-ray computed tomography images," *NDT and E International*, vol. 37, pp. 373–380, 7 2004.

[43] J. Zheng, Y. Sun, Z. Luo, and D. Zhang, "High precision post-processing framework for industrial computed tomography detection," *Expert Systems with Applications*, vol. 192, p. 116401, 2022.

[44] M. Busch and T. Hausotte, "Application of an edge detection algorithm for surface determination in industrial x-ray computed tomography," *Production Engineering*, vol. 16, pp. 411–422, 4 2022.

[45] R. Jiménez-Pacheco, S. Ontiveros, J. A. Yagüe-Fabra, F. Zanini, S. Carmignato, and J. A. Albajez, "Assessment of gradient-based algorithm for surface determination in multi-material gap measurements by x ray computed tomography," *Materials*, vol. 13, no. 24, p. 5650, 2020.

[46] Z. Zhang, F. Gao, and Q. Zhang, "Three-dimensional reconstruction of continuous tomographic ict images of defective srm," in *IOP Conference Series: Materials Science and Engineering*, vol. 816, p. 012009, IOP Publishing, 2020.

[47] J. Yagüe-Fabra, S. Ontiveros, R. Jiménez, S. Chitchian, G. Tosello, and S. Carmignato, "A 3d edge detection technique for surface extraction in computed tomography for dimensional metrology applications," *CIRP Annals*, vol. 62, no. 1, pp. 531–534, 2013.

[48] M. Sokac, M. Katic, Z. Santosi, D. Vukelic, I. Budak, and N. M. Durakbasa, "Investigation of influence by different segmentation parameters on surface accuracy in industrial x-ray computed tomography," pp. 202–209, Springer Science and Business Media Deutschland GmbH, 2022.

[49] X. Zhou, N. Dai, X. Cheng, A. Thompson, and R. Leach, "Intelligent classification for three-dimensional metal powder particles," *Powder Technology*, vol. 397, 1 2022.

[50] S. Jeon, S. Kim, and C. O. Lee, "Shape prior metal artefact reduction algorithm for industrial 3d cone beam ct," *Nondestructive Testing and Evaluation*, vol. 36, pp. 176–194, 2021.

[51] S. Lou, L. Pagani, W. Zeng, X. Jiang, and P. J. Scott, "Watershed segmentation of topographical features on freeform surfaces and its application to additively manufactured surfaces," *Precision Engineering*, vol. 63, pp. 177–186, 5 2020.

[52] M. Sokac, I. Budak, M. Katic, Z. Jakovljevic, Z. Santosi, and D. Vukelic, "Improved surface extraction of multi-material components for single-source industrial x-ray computed tomography," *Measurement*, vol. 153, p. 107438, 2020.

[53] L. Liu, L. Zeng, and X. Luan, "3d robust chan-vese model for industrial computed tomography volume data segmentation," *Optics and Lasers in Engineering*, vol. 51, pp. 1235–1244, 11 2013.

[54] L. Liu, L. Zeng, K. Shen, and X. Luan, "Exploiting local intensity information in chan-vese model for noisy image segmentation," *Signal Processing*, vol. 93, pp. 2709–2721, 9 2013.

[55] T. Mizoguchi, H. Date, S. Kanai, and T. Kishinami, "Quasi-optimal mesh segmentation via region growing/merging," 2007.

[56] J. Wang, Y.-P. Lu, and Y.-F. Cai, "The application of volumetric region growing in segmentation for volume data from industrial computed tomography," in *ICMIT 2005: Information Systems and Signal Processing*, vol. 6041, pp. 112–117, SPIE, 2006.

[57] R. Huang, K. L. Ma, P. McCormick, and W. Ward, "Visualizing industrial ct volume data for nondestructive testing applications," pp. 547–554, 2003.

[58] S. Liu and W. Ma, "Seed-growing segmentation of 3-d surfaces from ct-contour data," 1999.

[59] P. Fuchs, T. Kroeger, and C. S. Garbe, "Defect detection in ct scans of cast aluminum parts: a machine vision perspective," *Neurocomputing*, vol. 453, pp. 85–96, 2021.

[60] Z. Xiao, K.-Y. Song, and M. M. Gupta, "Development of a cnn edge detection model of noised x-ray images for enhanced performance of non-destructive testing," *Measurement*, vol. 174, p. 109012, 2021.

[61] C. J. Liu and X. L. Wu, "Industrial computerized tomography images segmentation based on cellular neural networks," in *Applied Mechanics and Materials*, vol. 66, pp. 2228–2235, Trans Tech Publ, 2011.

[62] N. Sakabe, Y. Ohtake, Y. Nagai, and H. Suzuki, "Identification of the number of overlapping welded thin plates in an x-ray ct volume," *Computer-Aided Design and Applications*, vol. 16, pp. 318–328, 2019.

[63] C. Yang, Y. Ohtake, M. Moriguchi, and H. Suzuki, "Generation of segmented triangular meshes from ct images based on centroidal voronoi tessellation and the graph cut method," *Journal of Computing and Information Science in Engineering*, vol. 14, 3 2014.

[64] Y. Ohtake and H. Suzuki, "Edge detection based multi-material interface extraction on industrial ct volumes," *Science China Information Sciences*, vol. 56, pp. 1–9, 9 2013.

[65] Y. Wen, S. Zhang, and Y. Zhang, "Detection and characterization method for interface bonding defects of new composite materials," *IEEE Access*, vol. 7, pp. 134330–134337, 2019.

[66] N. He, L. Zhang, and K. Lu, "Aluminum ct image defect detection based on segmentation and feature extraction," in *Design, User Experience, and Usability. User Experience Design for Diverse Interaction Platforms and Environments: Third*

International Conference, DUXU 2014, Held as Part of HCI International 2014, Heraklion, Crete, Greece, June 22-27, 2014, Proceedings, Part II 3, pp. 446–454, Springer, 2014.

[67] H. Boerner and H. Strecker, "Automated x-ray inspection of aluminum castings," *IEEE Transactions on Pattern Analysis and Machine Intelligence*, vol. 10, pp. 79–91, 1988.

[68] S. Suzuki, Y. Ohtake, and H. Suzuki, "Curvature gradient-estimation using ct sinogram and its application to reverse engineering," *CAD Computer Aided Design*, vol. 148, 7 2022.

[69] W. Cao, S. Hawker, G. Fardell, B. Price, and W. Dewulf, "An improved segmentation method for multi-material beam hardening correction in industrial x-ray computed tomography," *Measurement Science and Technology*, vol. 30, 9 2019.

[70] Y. Nagai, Y. Ohtake, and H. Suzuki, "Segmo: Ct volume segmentation using a multi-level morse complex," *CAD Computer Aided Design*, vol. 107, pp. 23–36, 2 2019.

[71] A. Jaiswal, M. A. Williams, A. Bhalerao, M. K. Tiwari, and J. M. Warnett, "Markov random field segmentation for industrial computed tomography with metal artefacts," *Journal of X-Ray Science and Technology*, vol. 26, pp. 573–591, 2018.

[72] H. Jiang, L. Zeng, and B. Bi, "A comprehensive method of contour extraction for industrial computed tomography images," *Optics and Lasers in Engineering*, vol. 51, pp. 286–293, 3 2013.

[73] H. E. Rushmeier, S. N. Spencer, A. D. Library., C. University, SIGGRAPH., E. A. for Computer Graphics., and A. for Computing Machinery, *Fuzzy CT Metrology:Dimensional Measurements on Uncertain Data*. 2013.

[74] B. He, F. Liu, and B. Bi, "Precise vectorization of industrial computed tomographic image," vol. 156-157, pp. 523–528, 2011.

[75] K. Wang, D. H. Zhang, X. B. Zhao, K. D. Huang, and Y. Y. Cheng, "Surface detection with subvoxel accuracy using facet model and iddg operator," 2006.

[76] X. Wua and W. G. Weea, "Surface detection with subvoxel accuracy using 3-d directional derivatives," 1999.

[77] G. A. Jones and P. Huthwaite, "Fast binary ct using fourier null space regularization (fnsr)," *Inverse Problems*, vol. 36, 2020.

[78] C. Chapdelaine, A. Mohammad-Djafari, N. Gac, and E. Parra, "A 3d bayesian

computed tomography reconstruction algorithm with gauss-markov-potts prior model and its application to real data," vol. 155, pp. 373–405, IOS Press, 2017.

[79] W. Zhang, H. Zhang, L. Li, L. Wang, A. Cai, Z. Li, and B. Yan, "A promising limited angular computed tomography reconstruction via segmentation based regional enhancement and total variation minimization," *Review of Scientific Instruments*, vol. 87, 8 2016.

[80] M. Sezgin and B. l. Sankur, "Survey over image thresholding techniques and quantitative performance evaluation," *Journal of Electronic imaging*, vol. 13, no. 1, pp. 146–168, 2004.

[81] R. Adams and L. Bischof, "Seeded region growing," *IEEE Transactions on pattern analysis and machine intelligence*, vol. 16, no. 6, pp. 641–647, 1994.

[82] S. Beucher, "Use of watersheds in contour detection," in *Proc. Int. Workshop on Image Processing, Sept. 1979*, pp. 17–21, 1979.

[83] T. F. Chan and L. A. Vese, "Active contours without edges," *IEEE Transactions on image processing*, vol. 10, no. 2, pp. 266–277, 2001.

[84] B. S. Institution, *Geometrical product specifications (GPS). Acceptance and reverification tests for coordinate measuring systems (CMS). Part 5, Coordinate measuring machines (CMMs) using single and multiple stylus contacting probing systems using discrete point and/or scanning measuring mode.*

[85] VolumeGraphics, "Vgstudiomax software." `https://www.volumegraphics.com/en/products/vgsm.html`.

[86] N. Phansalkar, S. More, A. Sabale, and M. Joshi, "Adaptive local thresholding for detection of nuclei in diversity stained cytology images," in *2011 International conference on communications and signal processing*, pp. 218–220, IEEE, 2011.

[87] R. van den Boomgaard, "Lecture notes image processing and computer vision." `https://staff.fnwi.uva.nl/r.vandenboomgaard/IPCV20172018/LectureNotes/index.html`, 2017.

[88] D. C. Montgomery, *Design and analysis of experiments*. John wiley & sons, 2017.

A | MATLAB Code

Phansalkar

```
function volN = phansalkarTH(vol)

   [dx,dy,dz] = size(vol);
   volR = rescale(vol);
   n=9;p=15;q=9;k=0.25;R=0.5;

   %Calculate the radius of the neighbourhood
   w = (n-1)/2;
   wBTH = ones(size(vol));

   %Process the image
   for i=w+1:dx-w
      for j=w+1:dy-w
          for h=w+1:dz-w
              %Extract the neighbourhood area
              block = volR(i-w:i+w,j-w:j+w,h-w:h+w);

              %Calculate the mean and standard deviation of the block
              mnB = mean(block, 'all');
              sdB = mean((block-mnB).^2, 'all').^0.5;

              %Calculate the threshold value
              ph = p * exp(-q * abs(mnB));
              wBTH(i,j,h) = (mnB * (1 + ph + k * ((sdB/R) - 1)));
          end
      end
   end
   volN = imbinarize(volR, wBTH);
end
```

Measurement of Diameter and Cylindricity

```
function [toll,parametri]=ctollbyfervs(X,r,xnom,anom,flag)

if nargin==1
    xnom=[0 0 0]';
    anom=[0 0 1]';
    [xls, als,r] = lscylinder(X, xnom(:),anom(:), 1, 1e-6, 1e-6);
    xls=xls';
    als=als';
elseif nargin==5 && flag==1
    [xls, als,r] = lscylinder(X, xnom(:),anom(:), r, 1e-6, 1e-6);
    xls=xls';
    als=als';
else
    xls=(xnom(:))';
    als=(anom(:))';
end
[tollatt,rintatt,rextatt]=stimaatt(X,xls,als);
limitxymin=r/100;% inizializzazione
limitthmin=2*pi/100;
limitth=limitthmin;
limitxy=limitxymin;
xin=xls;
ain=als;
flag=0;
count=0;
while flag==0
    [Xrot,matrot]=spostapunti(X,xin,ain);
    m=size(Xrot,1);
    vinclin(:,1:6)=[2*Xrot(:,1).*Xrot(:,3) 2*Xrot(:,2).*Xrot(:,3) 2*Xrot(:,1) 2*Xrot(:,2)...
        ones(m,1)*2*rintatt zeros(m,1)
        -2*Xrot(:,1).*Xrot(:,3) -2*Xrot(:,2).*Xrot(:,3) -2*Xrot(:,1) -2*Xrot(:,2)...
        zeros(m,1) -2*rextatt*ones(m,1)];
    lim=[-rintatt^2+Xrot(:,1).^2+Xrot(:,2).^2
        rextatt^2-Xrot(:,1).^2-Xrot(:,2).^2];
    lbound=[-limitth -limitth -limitxy -limitxy -inf -inf];
    ubound=[limitth limitth limitxy limitxy inf inf];
    options=optimset('maxiter',1000000,'display','off','LargeScale','off');
    paratt=fmincon(@distanza,[0 0 0 0 -tollatt/2 tollatt/2],vinclin,lim,[],[],...
        lbound,ubound,[],options);
    [xnew,anew]=nuovoasse(paratt(1),paratt(2),paratt(3),paratt(4),matrot,xin);
    [tollnew,rintnew,rextnew]=stimaatt(X,xnew,anew);
    if ((tollnew-tollatt)*2/(tollnew+tollatt))<-1e-9 && count<1000
        tollatt=tollnew;
```

```
        tollatt=tollnew;
        ain=anew;
        xin=xnew;
        count=count+1;
    elseif limitxy>limitxymin*10
        toll=tollatt;
        parametri=[xin(1) xin(2) xin(3) ain(1) ain(2) ain(3) (rintnew+rextnew)/2];
        flag=1;
    else
        limitxy=limitxy*2;
        limitth=limitth*2;
    end
end

function [Xrot,matrot]=spostapunti(X,xin,ain)
o=eye(3);
on=[0 -ain(3)/sqrt(ain(3)^2+ain(2)^2) ain(2)/sqrt(ain(3)^2+ain(2)^2)
    (ain(2)^2+ain(3)^2)/sqrt((ain(2)^2+ain(3)^2)^2+(ain(1)*ain(2))^2+(ain(1)*ain(3))^2)...
    -(ain(1)*ain(2))/sqrt((ain(2)^2+ain(3)^2)^2+(ain(1)*ain(2))^2+(ain(1)*ain(3))^2)...
    -(ain(1)*ain(3))/sqrt((ain(2)^2+ain(3)^2)^2+(ain(1)*ain(2))^2+(ain(1)*ain(3))^2)
    ain(1)/sqrt(ain(1)^2+ain(2)^2+ain(3)^2) ain(2)/sqrt(ain(1)^2+ain(2)^2+ain(3)^2)...
    ain(3)/sqrt(ain(1)^2+ain(2)^2+ain(3)^2)];
matrot=o*on';
xtrasl=[X(:,1)-xin(1) X(:,2)-xin(2) X(:,3)-xin(3)]';
xrotist=matrot'*xtrasl;
Xrot(:,1:3)=xrotist';

function [xnew,anew]=nuovoasse(dbe,dga,dx,dy,matrot,xin)
anew=matrot*[dbe dga 1]';
anew=anew/sqrt(anew'*anew);
point=matrot*[dx dy 0]';
xnew=point'+xin;

function [Toll,rintatt,rextatt,dist]=stimaatt(X,xatt,aatt)
m=size(X,1);
X=X-repmat(xatt,m,1);
dist=sqrt((aatt(2)*X(:,1)-aatt(1)*X(:,2)).^2+(aatt(1)*X(:,3)...
    -aatt(3)*X(:,1)).^2+(aatt(3)*X(:,2)-aatt(2)*X(:,3)).^2);
Toll=max(dist)-min(dist);
rintatt=min(dist);
rextatt=max(dist);
function [d]=distanza(x)
d=(x(6)-x(5));
```

Plane Distance

```
close all; clc

% identify the bottom cylinder
p = load('base_cop.mat'); fNames = fieldnames(p); p = p.(fNames{1});
p0 = lscylinder(p,[640;640;0],[0;0;1], 28, 1e-6, 1e-6); % cylinder axis point

% fit the top plane for his normal vector
p = load('plane_1.mat'); fNames = fieldnames(p); p = p.(fNames{1});
[x0,z] = lsplane(p);
% make sure z points upward
z = z*sign(z(3));

% determine the axis origin o
t = (z'*x0-z'*p0)/(z'*z);
o = p0+t*z;

% determine the five distances
d = zeros(5,1);
for h = 1:5
    % load the plane points and fit them
    p = load(['plane_' num2str(h+1) '.mat']); fNames = fieldnames(p); p = p.(fNames{1});
    [p0, n0] = lsplane(p); % lower plane
    p = load(['plane_' num2str(h) '.mat']); fNames = fieldnames(p); p = p.(fNames{1});
    [p5, n5] = lsplane(p); % upper plane
    % make sure the plane normals points upward
    n0 = n0*sign(n0(3));
    n5 = n0*sign(n5(3));
    % calculate the intersections
    t = (n5'*p5-n5'*o)/(n5'*z);
    pi5 = o+t*z;
    t = (n0'*p0-n0'*o)/(n0'*z);
    pi0 = o+t*z;
    % calculate the distance
    d(h) = -(pi0-pi5)'*n5;
end
```

Canny Subvoxel

```
 close all; clc

 % Load of raw volume and result of Canny segmentation
data = load(load_name); fNames = fieldnames(data); data = data.(fNames{1});
dataE = load(seg_name); fNames = fieldnames(dataE); dataE = dataE.(fNames{1});

%Gaussian smoothing on data
data = imgaussfilt3(data,sqrt(2));

% coordinate of the center of the segmented pixels
indice = find(dataE);
[ey,ex,ez] = ind2sub(size(dataE),indice);

% the aim is to implement the formula for the colculation of the numerator
% and denominator of the formula. So we need:
% numerator: fx^2fxx+2fxfyfxy+fy^2fyy
% denominator: fx^3fxxx+3fx^2fyfxxy+3fxfy^2fxyy+fy^3fyyy.
% as this would require a lot of memory, let's try to do this step by step,
% saving only the data we actually need

% first derivatives
[d1{1},d1{2},d1{3}] = imgradientxyz(data);
for h = 1:numel(d1)
    % keep only the required data
    d1{h} = d1{h}(dataE)./44;
end

% second derivatives
d2 = cell(3,3);
for h = 1:3 % the h index cycles on x,y
    d1t = cell(3,1);
    % calculate the first derivative and keep only the current one
    [d1t{1},d1t{2},d1t{3}] = imgradientxyz(data);
    d1t = d1t{h}./44;
    % calculate the second derivatives
    [d2t{1},d2t{2},d2t{3}] = imgradientxyz(d1t);
    for k = 1:3 % the k index cycles on x,y
        % keep only the required data
        d2{h,k} = d2t{k}(dataE)./44;
    end
end
```

```
% third derivatives
d3 = cell(3,3,3);
for h = 1:3 % the h index cycles on x,y
    d1t = cell(3,1);
    % calculate the first derivative and keep only the current one
    [d1t{1},d1t{2},d1t{3}] = imgradientxyz(data);
    d1t = d1t{h}./44;
    for k = 1:3 % the k index cycles on x,y
        d2t = cell(3,1);
        % calculate the second derivatives and keep only the current one
        [d2t{1},d2t{2},d2t{3}] = imgradientxyz(d1t);
        d2t = d2t{k}./44;
        % calculate the second derivatives
        [d3t{1},d3t{2},d3t{3}] = imgradientxyz(d2t);
        for u = 1:3 % the u index cycles on x,y
            % keep only the required data
            d3{h,k,u} = d3t{u}(dataE)./44;
        end
    end
end

% calculate numerator
% numerator: fx^2fxx+fy^2fyy+fz^2fzz+2fxfyfxy+2fxfzfxz+2fzfyfzy
numerator = zeros(size(ex));
for h = 1:3
    for k = 1:3
        numerator = numerator+d2{h,k}.*d1{h}.*d1{k};
    end
end
% calculate denominator
% denominator: fx^3fxxx+fy^3fyyy+fz^3fzzz+3fx^2fyfxxy+3fxfy^2fxyy+
% 3fx^2fzfxxz+3fxfz^2fxzz+3fz^2fyfzzy+3fzfy^2fzyy+3fzfyfzfxyz.
denominator = zeros(size(ex));
for h = 1:3
    for k = 1:3
        for u = 1:3
            denominator = denominator+d3{h,k,u}.*d1{h}.*d1{k}.*d1{u};
        end
    end
end
x = ex-numerator./denominator.*d1{1};
y = ey-numerator./denominator.*d1{2};
z = ez-numerator./denominator.*d1{3};
```

List of Figures

List of Tables

Acknowledgements

I would like to thank *Prof. Giovanni Moroni* for his help and advices throughout the research activity and for providing me with the opportunity to conduct my thesis within his research group, where I had the opportunity to learn a lot.

I am particularly grateful to *Prof. Stefano Petrò* for his constant availability, attentiveness, and patience throughout the duration of my thesis.

Additionally, I would like to thank *Dr. Huan Shao* for his guidance, support, and trust in me during these past months.

Finally, I wanted to thank my sister *Valentina* and *my entire family* for supporting and encouraging me throughout these years.